Post-Print

This is the accepted version of:

F. Piscaglia, F. Giussani, J. Hèlie, N. Lamarque, S.M. Aithal
Vortex Flow and Cavitation in Liquid Injection: a Comparison Between High-Fidelity CFD Simulations and Experimental Visualizations on Transparent Nozzle Replicas
International Journal of Multiphase Flow, In press - Published online 17/02/2021
doi:10.1016/j.ijmultiphaseflow.2021.103605

The final publication is available at https://doi.org/10.1016/j.ijmultiphaseflow.2021.103605

Access to the published version may require subscription.

Highlights

1. CFD simulation performed from a virtual model of the real injector directly built from XCT;
2. vortex strings generation in the injectors are related to the flow pattern in the sac;
3. a non-dimensional parameter is proposed to characterize the flow in the injector sac;
4. the non-axial kinetic energy in the nozzle is linked to the intensity of cavitation;
5. flow unsteadiness and vortex pair instabilities influence the flow topology.

Vortex Flow and Cavitation in Liquid Injection: a Comparison between High-Fidelity CFD Simulations and Experimental Visualizations on Transparent Nozzle Replicas

F. Piscaglia[a], F. Giussani[a,b], J. Hèlie[b], N. Lamarque[b], S. M. Aithal[c]

[a]*Dept. of Aerospace Science and Technology (DAER), Politecnico di Milano, Italy*
[b]*Vitesco Technologies (Continental AG Group), France*
[c]*Argonne National Laboratory, Lemont, US*

Abstract

Experimental instantaneous shadowgraph visualizations on transparent glass nozzle replica of high-pressure fuel injectors have been used to validate a novel in-house developed high-fidelity LES-VOF multiphase solver, to study the evolution of vortex flow and fuel cavitation. Both experiments and simulations capture the formation of an unsteady vapor structure inside the nozzle volume, which is referred to as 'string-cavitation'; strings are found at the core of the recirculation zones. High-fidelity simulations provide a very detailed insight into the vortex generation in the injector nozzle; strings appear within the time scales that are relevant for fast injection events (on the order of 0.1 milliseconds) and, for the problem under consideration, their generation seems mostly related to the flow pattern in the sac. It is also shown that vortexes interact, merge till they disrupt and favor the temporary inception of shear cavitation.

Key words: 3-phase LES-VOF solver, CFD of internal nozzle flows, cavitation, liquid injection, primary atomization, OpenFOAM, LibPoliMi/DAER

1. Introduction

The study of atomization in liquid injection is a rapidly developing field of broad importance. There are many interesting applications of spray theory related to aeronautics, power, propulsion, heat transfer and materials processing. The flow inside the nozzle, guided by the injector design, has a dominant effect on the generation of spray patterns and propellant-air mixing. Optimal design of the injector geometry enables one to control the spray patterns and hence

*Corresponding author: federico.piscaglia@polimi.it

ultimately control the combustion efficiency. This is especially true in the presence of cavitation, where the flow field inside the nozzle must be regulated to maximize the available liquid surface area at the nozzle exit to facilitate mass, momentum and heat transfer. Cavitation plays a pivotal role in achieving finer atomization of the spray, enabling improved fuel economy and reduced emission levels during combustion [1, 2]; however, cavitation may limit the stability of the spray [3] and potentially damage the injector components, leading to reduced reliability of the injector. In injector nozzles, surface spots initially surrounded by a cavitating flow region tend to erode at an accelerated pace: cavitation pits increase the turbulence of the flow and create crevices that act as nucleation sites for new cavitation bubbles, thus leading to an avalanche effect. For the above mentioned reasons, the study of internal nozzle flows in injectors is essential. However, characterization of the flow inside the nozzle is difficult, both experimentally and numerically. Non-invasive experimental measurements are difficult on account of the high pressures and small sizes. Experimental studies on scaled (enlarged) geometries and reduced pressures do not provide meaningful insights of the flow characteristics and hence are of limited usefulness. Very few examples of detailed numerical studies with validation against experiments on internal flows in actual nozzles under realistic operating conditions are available in the literature [4, 5, 6]. Numerical simulations of such flows are difficult not only because they require robust numerical schemes and models to accurately capture the turbulent, multiphase nature of the flows (liquid fuel, gaseous fuel and air) but also large computational resources to compute the long transients with high-resolution grids capable of capturing the sharp liquid/vapor interfaces. Despite these challenges, various researchers have sought to study injector flows using experimental and numerical methods. Given the micron-sized dimensions of these nozzles, Particle Image Velocimetry (PIV) and Laser Doppler Velocimetry (LDV) are rarely available in the nozzle orifice and in the primary breakup region [7, 8, 9, 10, 11, 12, 13]. Typically, flow visualization is done using shadowgraph techniques with modern high speed cameras on transparent replicas [14, 15, 16, 17]. Andriotis et. al [16] reported studies on large injector from propulsion systems for marine applications, being the construction of replicas easier. Standard shadowgraphy (illumination from above) on an internal nozzle flow of an asymmetric prototype of a glass nozzle has been published in [17]. Studies of fully transparent replicas of high-pressure injector nozzles under actual operating conditions (100 - 2000 bars) have been reported [14, 15, 18, 19]. In [18], the influence of the relative position of the holes and the hole-to-hole interactions on string cavitation was investigated in a real-scale nozzle for pressures up to 2000 bar. There are a relatively fewer simulations of flows in nozzle injectors under realistic operating conditions and geometries [20, 21]. In [20], enlarged replicas of Valve Covered Orifice-type (VCO) injectors incorporating tapered converging holes were simulated; a similar study has been published in [21], where the solver handled the presence of multiple phases using the homogeneous equilibrium model [22], to calculate the compressibility of the liquid/vapor mixture. Most of the experimental tests to investigate cavitation in high-pressure liquid injection were done by observing the similarity laws. Nozzles were built as large as possible (geometrical similarity); also, same Reynolds numbers (dynamical similarity), same cavitation numbers (cavitation similarity) and same Weber number were preserved. Unfortunately, being cavitation a multi-scale effect due to bubble growth from nuclei sizes, it cannot be scaled up [23]. The first realization of real size nozzles was a great step toward a more representative transparent nozzle which compares good to real parts. Simplified realistic size two-dimensional holes were initially considered in [24] and are still useful for basic simulation model validation or well-controlled optical measurements [25]. In [26], it was found that visualizations are more sensitive than mass flow rate measurement: cavitation inception occurs prior to the change in mass flow rate, and bubbles are observed in the spray area even in absence of choked flow. The hole inlet radius was identified to strongly influence the cavitation inception and the flow detachment at the hole inlet edge as the flow's direction turns toward the hole. Finally, in [8] it is shown that the cavitation length increases with the injection pressure and that cavitation collapse at the vicinity of the hole exit improves atomization. At higher cavitation numbers, when the cavitation zone is reaching the hole exit, the air can propagate back in the nozzle; air fills part of the volume that would be taken by the vapor, reducing the amount of cavitation and stabilizing the gaseous flow area. This so-called hydraulic flip limits the intensity of the atomization and stabilizes the flow [8, 24]. The limit of two-dimensional holes is driven by the two-dimensional cavity depth. If too small, the influence of the boundary will not be negligible; if too deep, the shadowgraph visualization will be integrated along the whole optical path and it is the result of a superimposition of multiple bubbles developing at different depths. The signal absorption saturates even with low density of cavitation and in moderate regimes. It is then almost impossible to distinguish different vapor density levels. It is thus useful to use more complex X-Ray measurements. Another aspect which cannot be fulfilled by two-dimensional nozzles is the fluid velocity at needle seat and towards the sac geometry as found in real nozzles. The reason is that the flow area along the flow line is usually becoming smaller due to the conical geometry around the seat and the sac, that cannot be represented in two dimensions. Many authors investigated central axisymmetric holes that are more realistic in terms of geometry scale. However, visualization of axisymmetric holes is also difficult. Finally, in central two-dimensional channel or axisymmetric holes, the fluid is cavitating uniformly with a stable behavior, whereas the observed regimes

of asymmetrical nozzles with non divergent holes (like supercavitation) are mostly unstable. Therefore, asymmetrical inlet conditions and inclined holes were then studied [11]. Recent publications report building and measurements of a realistic shape of transparent nozzles using one simple rectangular insert with the flow hole inside. Some authors succeeded to integrate it in a real metal nozzle [18], or to produce an even more complex shape fully transparent [27]. However, keeping the nominal geometry or managing a complex shape when considering real-size nozzles and high-pressure conditions becomes very difficult. No real proof of concept of realistic nozzles that are exhibiting the former qualities while being at the same time compatible with rapid prototyping approach has been demonstrated until now to our knowledge. A proof of concept of a real-size, real-shape, real-pressure, representative surface roughness, transparent nozzles for Design of Experiments, is used to validate a LES-VOF solver developed by the authors in [28].

The aim of this work is to conduct a systematic study, both experimentally and numerically, of the flow characteristics in high pressure liquid injectors working under typical operating conditions. Two different configurations of real-size transparent glass-nozzle replicas of injectors were built by Vitesco Technologies for this study [29]. Nozzle replicas have been realized using a novel rapid prototyping technique using laser-etched manufacturing and presented in [29]. The aim of the experiments was to provide a detailed visualization of the in-nozzle flow and of the extent primary jet breakup. Tests have been carried out sequentially by using a camera to produce shadowgraph images for two different viewing, namely the front view and the lateral view, in order to obtain well resolved three-dimensional visualization of the flow characteristics. High-resolution simulations of the injector flows were conducted using an in-house Finite Volume (FV) variable-density multiphase VOF solver developed by the authors. The solver used in this study [28] is developed in the OpenFOAM Technology and it is included in a in-house C++ library developed by the authors. Validated results from the simulations were post-processed to investigate the physical mechanism leading to the flow instability inside the nozzle. The experiments (and simulations) were conducted using n-Heptane as the injected liquid fuel at a pressure of 100 bar.

The paper is organized as follows: Sec. 2 discusses the phenomenological process of flow and cavitation in real world injectors operating at high pressures. A discussion of the experimental and measurement procedure is included in Sec. 3. The simulation methodologies used in multiphase (liquid and gas), multi-component (fuel and air in gaseous phase) flows as it pertains to injector and the main equations of the variable-density flow solver implemented and verified in [28] are discussed in Sec. 4. Simulation results using the solver of [28] are validated against the instantaneous shadowgraph pictures from experiments in Sec. 5, to prove the reliability of the solver to describe the cavitating structures occurring in the real glass nozzle injectors. Sections 6-7 discuss the simulation results. The main phenomena influencing the primary break-up mechanisms, generated inside the nozzle orifices, are identified into two sources: cavitation and flow dynamics, which are the subjects of the present work. Primary breakup mechanism is not analyzed in this work and it will be the topic of further publications. Conclusions are drawn in Sec. 10.

2. Phenomenological process of flow and cavitation in high pressure injectors

Two different forms of cavitation have been distinguished [30, 31] and they are known as “geometry-induced” (or shear) and “string” (or vortex) cavitation respectively. Shear cavitation is initiated at sharp corners where the pressure falls below the saturation value [32, 33, 34] because of a sudden flow detachment and the accompanying recirculation region. For a given injector geometry, as the injection pressure increases, the region of cavitation grows and extends to the outlet until supercavitation occurs. The growth of the cavitation region increases the turbulence and spray angle of the jet [8, 35]. During this process, the liquid jet atomization is enhanced [35]. Increasing the injection pressure beyond a critical value leads to a “hydraulic flip”, wherein the air surrounding the nozzle outlet is sucked into the nozzle orifice to fill the cavitation area which makes the cavitation disappear immediately as a thin layer of gas is attached to the wall [36]. This occurrence is not beneficial for the atomization and can badly affect the fuel injector performance as a decrease of the spray cone angle is usually observed in this situation [36]. However, real nozzles are not completely smooth and symmetrical on account of the manufacturing process and hence maintaining a stable hydraulic flip is difficult. Thus, the phenomenon of local reattachment will occur periodically. String (or vortex) cavitation, conversely, develops by the evolution of the vorticity which allows the formation of geometry-scale vortices and is significantly influenced by the walls and the interaction with other vortices [15]; additionally, low pressure regions in the centers of the vortexes in the nozzle can generate a phase-change or entrap and stabilize bubbles that were entrained in their proximity, similarly to what is observed in hydro-machines [37, 38]. Vortex cavitation in the injector nozzles was first observed by Kim [39] and since then it has been described in further studies performed in enlarged nozzle replicas and was termed also as “string cavitation” [16, 40]. The main differences between vortex cavitation in propellers and turbines and those in fuel injectors arise from the geometric size and operating conditions. Nozzle flows develop in very confined volumes (nozzle geometries are on the order of a few

hundred microns) and at high pressures (> 100 atm) whereas turbines and propellers have much larger geometrical sizes and lower operating pressures. In nozzle flows, the high operating pressures and small geometrical size may allow formation of vortexes whose sizes are large relative to the nozzle geometry and where each cavitating vortex may interfere with other vortexes. In these small sized nozzles the proximity of the walls can also significantly impact the formation and structure of these vortexes. Additionally, large pressure drops in fuel injectors are encountered within very short distances (few hundreds of micrometers) while the lifetime of the formed vortical structure is usually only a fraction of the injection period. Cavitation strings are usually formed during fuel injection in areas where large-scale vortical structures develop: this happens when local pressure level is lower than the vapor pressure of the fuel. In a typical nozzle geometry, cavitation vortices are located between the separation point on the needle surface and the separation point at the hole inlet corner, and where there is sharp flow turning inside the sac volume of the injector. Unlike geometrical cavitation, string cavitation is present in any nozzle geometry: with sac-type and VCO nozzles and with either cylindrical or tapered holes, whose inlet can be either sharp or rounded. This has raised questions about the existence of vaporized liquid inside large-scale vortical structures; more recent studies [16, 41] suggest that string cavitation represents a transport process of vapor carried by the vortex flow rather than a phase-change process. Formation of string cavitation would originate from pre-existing (shear) cavitation sites, forming a continuous vapor column that extends into the flow region between adjacent holes. This can explain the presence of vapor where the pressure is quite high, for instance in the sac volume between holes. The underlying physics of confined vortex cavitation and of its onset in high pressure injectors still remains unclear and not yet fully understood. In this sense, the combination of shadowgraph visualizations on real-size transparent nozzle replicas and high-fidelity simulations can help to improve the understanding about this complex flow physics.

3. Experimental setup

Ad-hoc prototypes of real-sized glass nozzle injectors used for this study are capable of operating under realistic nozzle pressures; they were designed and built by Vitesco Technologies to contribute to the nozzle design and cavitation control efforts aimed at improving high-pressure fuel injectors [29]. The geometrical features of the prototype have been thought to reproduce a single-hole injector, representing a 60^o sector of a real multi-hole injector, as reported in Fig. 2. This includes the needle, the sac geometry, the hole geometry and the external nozzle shape.

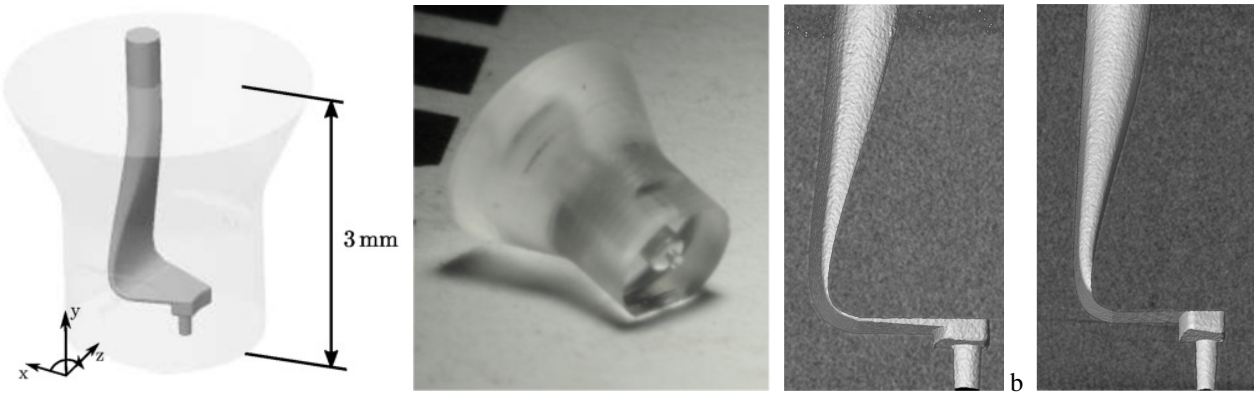

Figure 1: Sample of transparent glass nozzle replica: a) external view; b) sample of a central-nozzle hole; c) XCT visualization of glass nozzle side of ID-3; d) XCT visualization of glass nozzle side of ID-10

The injector prototype has been built in quartz glass (fused silica) by a laser-etched manufacturing process [29] that is able to achieve an average surface roughness of $1 - 3\ \mu m$. This surface roughness is typical of micro-EDM (Electrical Discharge Machining) processes used for manufacturing real injectors (A sample is shown in Fig. 1b). The nozzle can withstand pressure up to 350 bar and is compatible with any working fluid. The sector angle is slightly enlarged to allow the 60 ^{o} flow, while the side wall and the single hole are modifications when compared to real injectors. The injector geometry has been measured by a multisensor coordinate measuring machine based on a X-ray computed tomography (see Fig. 1c and Fig. 1d), to ensure the quality of the manufacturing process and

the correspondence between simulated and experimental geometry. The XCT is a V Tome XS 240 kV from General Electric. The nano-focus, 180 kV X-Ray tubes at 18 W (maximum power) has been used together with a tungsten-synthetic diamond target. XCT measurements are shown in Fig. 1 and the design values confirmed by XCT are presented in the table of Fig. 2.

Table 1: Thermodynamic properties for n − Heptane$_{(liq)}$, n − Heptane$_{(vap)}$ at T=25^o C, and non-condensable gas (air) at T=15^o C.

Parameter	Fluid		
	n − Heptane$_{(liq)}$	n − Heptane$_{(vap)}$	air
density ρ_l [kgm^{-3}]	684	4.25	1.225
dynamic viscosity μ_l [kg m^{-1} s^{-1}]	4.0835×10^{-4}	7.0125×10^{-6}	1.7885×10^{-5}
surface tension [Nm^{-1}]	0.019517	-	-
saturation pressure [Pa]	7000	-	-

Experiments have been carried out at Vitesco Technologies at the facility in Toulouse (France). The aim of the experiments was to provide a detailed visualization of the flow within the nozzle and the extent of the primary jet breakup. Experimental tests of liquid-into-air injection have been carried out at a needle lift of 79 μm, that is representative of a fully opened nozzle using n-Heptane as the working fluid, (both the numerical solver and the test bench can work with real fuels and are not limited to n-Heptane). The thermophysical and transport properties of n-Heptane are listed in Tab. 1. Tests have been carried out using a camera for two different viewing angles, $\theta_1 = 0^o$ (front view) and $\theta_2 = 90^o$ (lateral view), θ being the azimuthal angle. The flow solver described in [28] has been validated on two glass-nozzle configurations based on their individual jet penetrations. The average jet penetration over twenty experiments of ten different geometrical configurations (ID-1 to ID-10) was measured. Configurations ID-3 and ID-10 (see Fig. 2) showed respectively the maximum and minimum penetrations in the injection time interval (1400 μs) tested; these configurations were hence chosen for numerical validation and analysis. They have identical lift and similar values of nozzle inlet and outlet diameters. They are designed to deliver similar mass flow rate, but with different: a) nozzle sac geometry, through the height of the step H, the hole offset (off-H) and the length of the dead space; b) nozzle length. They operate at the conditions reported in Tab. 2.

Parameter	ID-10	ID-3	Unit
p_{inlet}	100	100	bar
p_{amb}	1	1	bar
Mean liquid Velocity U_l	155.07	149.43	m s^{-1}
Re at plane N_6	36110	35104	-
Re at plane S_1	14499	13020	-
K	1.0095	1.0095	-
C	104.9422	104.9422	-
We	110049	104712	-

Table 2: Operating conditions of the experimental tests applied to nozzle configurations ID-3 and ID-10 on plane N_6 of Fig. 6.

The fuel supply system consists of a low-pressure electrical pump, a heat exchanger, a high pressure pump, a common rail to damp oscillations, a fuel supply line with a pressure sensor to the injector valve along with the transparent testing nozzle. In the present work, the inlet fuel pressure has been set to 100 bar. The outlet of the nozzle is ambient temperature and pressure. While the solver assumes isothermal conditions of the working fluid, Tab. 1 reports the fluid properties computed at two different temperatures. In experiments usually n-Heptane and air have different temperatures: n-Heptane is usually warmer, at $\approx 25^oC$, while air in the injection chamber stays at $\approx 15^oC$. Under the isothermal approximation, the sensible heat exchange that would have been occurred during fuel-air mixing is neglected.

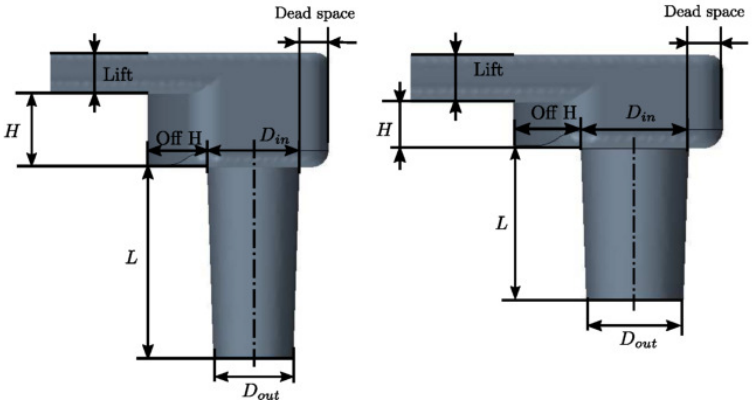

	Length [μm]	
	ID-3	ID-10
lift	80	79
nozzle length (L)	351	241
sac height (H)	136	78.5
hole offset (off-H)	102	78.5
inlet diameter (D_{in})	166	165
outlet diameter (D_{out})	147	148
dead space length	38	44.9
$K_{geom} = \left(\frac{D_{in}-D_{out}}{L}\right) \cdot 100$	12.92	10.52

Figure 2: The nozzle geometries studied, named as configuration ID-3 (left), ID-10 (right). Dimensions are specified in the Table.

Operating conditions for the flow were characterized on the basis of the following parameters:

- the cavitation number K, according to the definition of Nurick [27]:

$$K = \frac{p_{inj} - p_{sat}}{p_{inj} - p_{back}} \tag{1}$$

- the cavitation number C, according to the definition of Bergwerk [42]:

$$C = \frac{p_{inj} - p_{back}}{p_{back} - p_{sat}} \tag{2}$$

- the liquid Reynolds number (Re_l):

$$Re_l = \frac{\rho_l U_l D}{\mu_l} \tag{3}$$

with p_{inj} being the fuel injection pressure, p_{back} the pressure of the chamber, p_{sat} the saturation pressure of the liquid, ρ_l the density of liquid n-Heptane, D is the hydraulic diameter; U_l the mean liquid velocity, defined as:

$$\mathbf{U}_l = \frac{< \dot{m} >}{\rho_l A_{N_6}} \tag{4}$$

In Eq. (4), A_{N_6} is the cross-sectional area of plane N_6 in the nozzle hole (see Fig. 6), ρ_l is the density of liquid n-Heptane and $< \dot{m} >$ is the time-averaged mass flow rate (MFR) from experiments.

4. Computational Methodology for the Simulation of Cavitation in High-Pressure Injectors

CFD simulations have been performed on the XCT-based virtual model of the real component, rather than on the ideal CAD geometry. The workflow of the combined XCT–CFD procedure is summarized in Fig. 3. It is important to mention that the effect of the surface roughness is not accounted in the CFD simulations: despite the grid used is quite fine (80 M cells), it is still not fine enough to account for the influence of the roughness on the evolution of the boundary layers on the walls at the Reynolds numbers studied. It is worth mentioning that high resolution XCT cannot properly capture sharp edges; this may be a serious limit when dealing with injectors, because sharpness of the edges strongly influences the development of cavitation at the nozzle entrance. To correct this bias, measurements using a microscope were therefore used to quantify the hole edge rounding and to verify the average wall roughness (that were both found to be about 1 μm). Manual corrections were therefore applied to the CAD file in proximity of the sharp corners at the nozzle entrance, where information from the microscope were available.

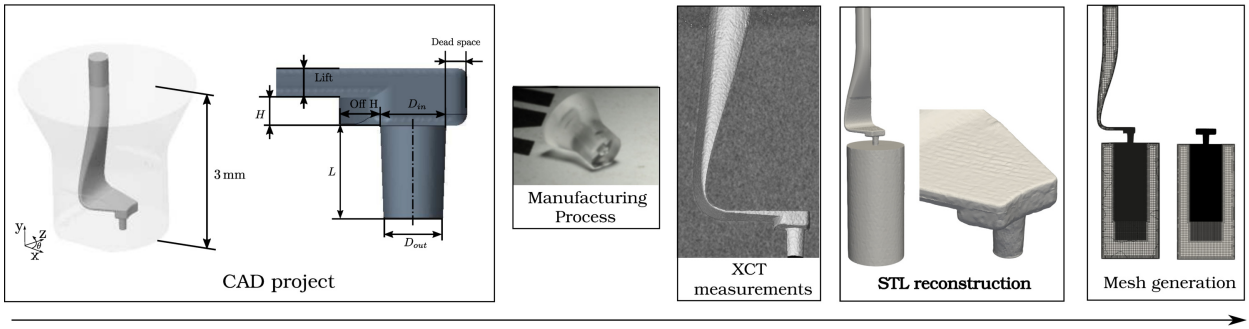

Figure 3: Sketch of the workflow for the generation XCT-based virtual model of the injectors studied. Since high resolution XCT cannot properly capture sharp edges, measurements from the microscope were used to quantify the hole edge rounding at the nozzle entrance. Manual corrections in the STL file, before the automatic generation of the polyhedral mesh.

The grid consists of 80 million of polyhedral cells, that allow different refinement levels in the different regions of the injector geometry, as shown in Fig. 3. The nozzle region is followed by an open cylindrical reservoir (a portion of the ambient volume where injection takes place) with different cell refinement levels. The finest refinement region in the grid has an average cell size of about 3 μm and it covers the sac, the nozzle and part of the reservoir, where primary atomization takes place. The selected cell size in this region is assumed to be sufficient to capture the finest ligament structures in the primary breakup region, that from experimental visualization was found to be in between 10 and 15 μm for the injectors studied. A region with average cell size of 8 μm is used in between the fine and the coarse regions of the grid and it is located in the reservoir, near the outlet of the domain. Finally, the coarse cell region has an average cell size of 40 μm and it is used where the flow is fully liquid (nozzle inlet) and in the buffer regions.

A three-phase variable-density multiphase VOF solver developed by the authors [28] for three fluids, two of which are miscible is used in this work. The three fluids are liquid fuel, fuel vapor and air (non-condensable gas). Fuel vapor and air are considered to be miscible fluids. The solver includes support for phase-change (fuel cavitation/condensation) by the implementation of the model by Schnerr and Sauer [43] with the extensions proposed by Yuan [44]. The cavitating fluid, the vapor and the non-condensable gas in the three-phase flow are represented in a single-fluid approximation as a mixture of phases, in which the phase-fraction distribution includes a sharp yet resolved transition between the phases. An algebraic-type VOF method belonging to the family of the interface-capturing methods [45] is used to capture the interface. Specifically, the interface is visualized by the contour of a scalar function, that is assumed to be the iso-value (set to 0.5 in this work) of the void fraction of the phase considered. Each phase i has a partial volume V_i, that is a fraction of the volume V of the cell element ($V_i \subseteq V$) and it is defined by its local volume fraction $\alpha_i \in [0;1]$:

$$\alpha_i = \frac{V_i}{V} \tag{5}$$

with:

$$\sum_{i=1}^{3} \alpha_i = 1 \tag{6}$$

a “mixture” density:

$$\rho = \sum_i \alpha_i \rho_i \tag{7}$$

and a “mixture” viscosity:

$$\mu = \sum_i \alpha_i \mu_i \tag{8}$$

It is important to note that density in the solver varies with pressure, through the phase transport equations. The flow is assumed to be isothermal. The effect of the heat transfer on the temperature, that can be accounted by solving the energy equation, is not considered in the present work. As mentioned earlier, the difference in the liquid fuel and air temperature is about 10 K justifying the isothermal assumption. The complete system of equations for three-phase flow with phase change are the phase-fraction equations, that are written as:

$$\begin{cases} \dfrac{\partial \alpha_l}{\partial t} + \nabla \cdot (\mathbf{U}\alpha_l) = -\dfrac{S_\alpha}{\rho_l} \\ \dfrac{\partial \alpha_v}{\partial t} + \nabla \cdot (\mathbf{U}\alpha_v) = \dfrac{S_\alpha}{\rho_v} \\ \dfrac{\partial \alpha_{nc}}{\partial t} + \nabla \cdot (\mathbf{U}\alpha_{nc}) = 0 \end{cases} \tag{9}$$

In the system of equations (9), S_α is a source term to model the phase-change (cavitation or condensation) at the liquid interface through the cavitation model and couples the effects of the cavitation with the evolution of the interface directly:

$$S_\alpha = \frac{\rho_v \rho_l}{\rho + \alpha_{nc}(\rho_l - \rho_{nc})} \frac{D\alpha_v}{Dt} \tag{10}$$

In Eq. (10) the subscripts l and v denote the liquid and vapor (that are involved in the phase change) respectively, while the subscript nc denotes the non-condensable gases (air). It is important to note that the closure of the system of equations (9) in presence of a cavitation/condensation source term S_α requires the explicit solution of a transport equation describing the third phase fraction (non-condensable phase). The solution of the transport equation describing the third fraction enables the inclusion of the cavitation model and the coupling of the equations with the compatibility condition (6). This procedure ensures that the system is closed and implicitly bounded on account of (6). In absence of source terms, 3-phase VOF solvers usually calculate the void fraction of non-condensable gases directly from Eq. (6), that is sufficient for closure only in that case. These aspects of the solution procedure are discussed in detail in [28], where the derivation of the full system of equations is shown and the formulation of the source terms for the phase change is also described. The discretization of the governing equations in the solver is based on the Finite-Volume (FV) approach as implemented in OpenFOAM [46]. Mass and momentum are solved using the pressure-implicit split-operator (PISO) algorithm [47]. Source terms for phase-change have been included in a semi-implicit formulation of the phase-fraction equations, where a flux corrected transport technique [48] is used to preserve boundedness of the solution. Detailed information about the solver is reported in [28].

LES turbulence modeling is used for the simulations, despite of its high computational cost, because of its better ability to characterize the different flow scales and therefore to capture the cavitation onset in the nozzle [49, 50, 51, 52, 53, 54, 55]. Unsteady Reynolds Averaged Navier-Stokes (URANS) methods can significantly underestimate the formation and the extent of cavitation, because they usually overestimate the turbulent viscosity in the cavitating regions [56, 57, 58, 59, 60]; a possible solution to overcome the limitations of URANS to model cavitation consists of reduce the eddy-viscosity predicted by the turbulence model [56]. Synthetic turbulence fluctuations were applied to initialize the internal flow field and replicate the initial conditions of the stagnant air in the reservoir, according to the method implemented in [61].

In [62], several numerical results of primary breakup using an Adaptive Mesh Refinement (AMR) technique show fairly good agreement with experimental data. The multiphase solver used in this work is able to support dynamically load-balanced Adaptive Mesh Refinement (AMR), but the authors chose to use a static polyhedral grid because: a) dynamic refinement/coarsening being a topological change, it has a negative impact on the accuracy of the calculation of the temporal derivatives (see Appendix A of [63]); b) the operation of the LES filtering would change with the dynamic topological change of the mesh due to the AMR [63, 64]; c) in the LES simulations presented in this work, the initial grid is very fine: even with load balancing, AMR would have a non-negligible impact on the simulation time, because it requires the mesh connectivity to be updated with each mesh refinement. Furthermore, even though the solver supports dynamic load balancing with AMR, one has to set practical limits of load unbalance among processors (usually 25% imbalance) to avoid excessive wall time spent in attaining the optimal load balance, especially for simulations with large grid sizes. Due to these considerations, the use of fine static grids is chosen in this work. Full detail about the numerical setup used for the simulations is described and discussed in [28].

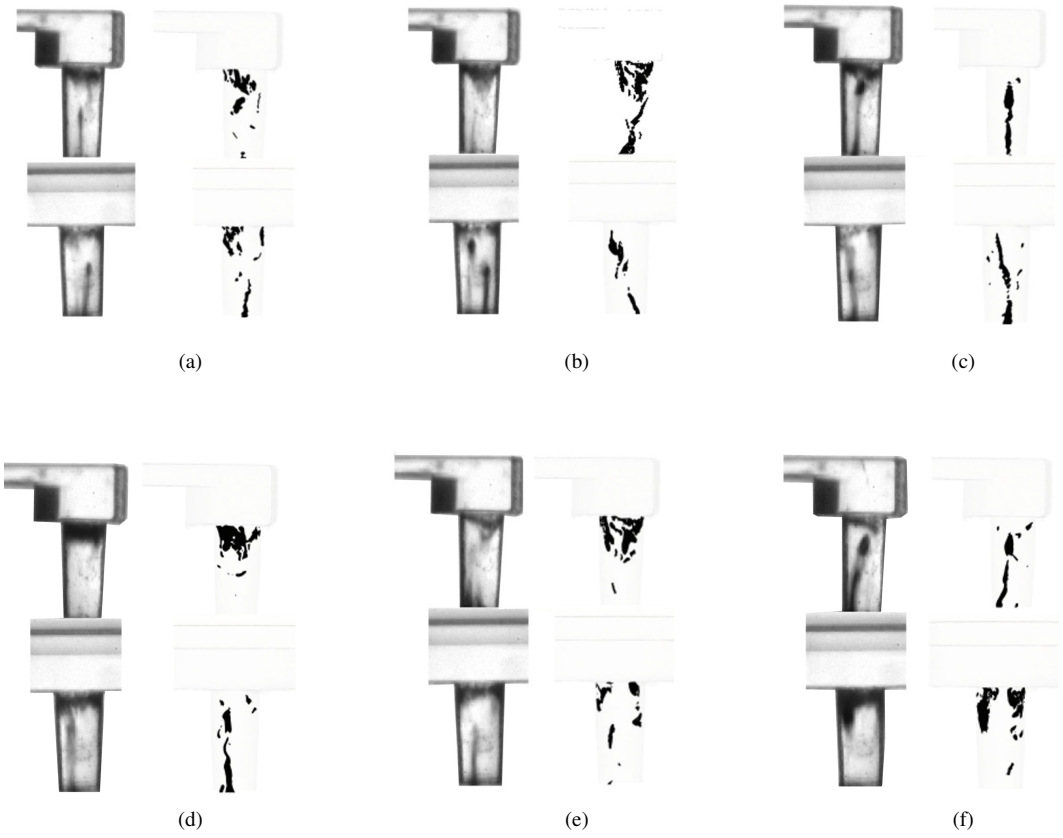

Figure 4: Configuration ID-3. Comparison of detected cavitation structures from experimental instantaneous shadowgraphies (left) and numerical simulations (right). Rows 1, 3: lateral view ($\theta = 90^o$). Rows 2, 4: front view ($\theta = 0^o$).

5. Validation

A validation by the comparison with experiments is presented, to prove the reliability of the solver to describe the cavitating structures occurring in the real glass nozzle injector. Experimental shadowgraph pictures of the cavitating areas have been realized using a long-range microscope (Navitar with home-made tubes from RDvision company) on the glass nozzle. A half-inch flexible fiber optic light guide mated with a powerful LED illuminator (white steady light). The camera is typically used with a exposure time of 2 μ seconds, but it is also possible to use a non coherent light with a very short duration of the illumination (about 10 ns). Bubbles appear dark in the image, while liquid regions appear bright. The experimental setup and the measurements are described in [29].

Simulations results are generated as projected views of the three-dimensional iso-surfaces ($\alpha_v = 0.3$) of the fuel-vapor.

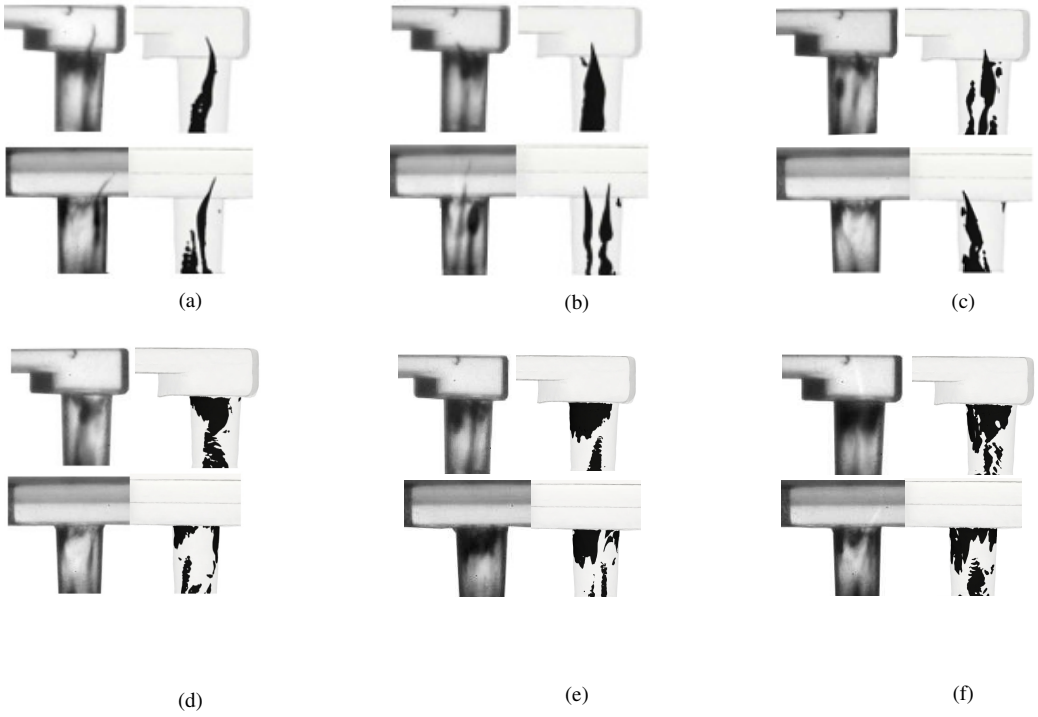

Figure 5: Configuration ID-10. Comparison of detected cavitation structures from experimental instantaneous shadowgraphies (left) and numerical simulations (right). Rows 1, 3: lateral view ($\theta = 90^o$). Rows 2, 4: front view ($\theta = 0^o$).

We report a comparison of numerical and experimental results on the front ($\theta = 0^o$) and lateral (side) view ($\theta = 90^o$) for the two injector configurations studied in this work. This kind of analysis can give a measure of reliability of the solver in describing the cavitating structures occurring inside the nozzle. In Figs. 4 and 5, a selection of instantaneous events from simulations and experiments are compared. The experimental visualizations using the front and lateral view are helpful to understand the contribution of each type of cavitation and the multiphase flow topology of each zone. Two different sets of images, namely a front ($\theta = 0^o$) and a lateral view ($\theta = 90^o$) have been realized by turning the injector sample around its axis. The flow through the two nozzles exhibits a moderate amount of cavitation, rarely noticed in the literature at the Cavitation and Reynolds numbers at which the injectors are operating (see Tab. 2). Central holes typically exhibit a circular, axisymmetric shear cavitation that develop over the section [29]; turning holes typically exhibit a large asymmetric single-side cavitation area [17, 65, 66]. In the cases studied, a moderate shear cavitation appears quite rarely, randomly, and it often involves a small portion of the nozzle area. Shear cavitation is directly driven by the low pressure area in the detached flow region in proximity of the hole entrance. Being the sharpness of the edge at the hole entrance directly linked to the intensity of the cavitation, the sharp edges at the hole entrance in the XCT-based virtual model have been manipulated by a CAD software; this ensures to be coherent with the measurements at the microscope and to cancel out the possible errors coming from the XCT-based reconstruction of the virtual model on those regions. The geometry has also been directly measured to generate the CAD, capturing some discrepancy in the asymmetry of the hole entrance. Few aspects help to explain this moderate shear cavitation in the two injector configurations. The geometry is a sector of a complex real nozzle: the shape includes a confined, non-negligible sac area. The role of the initial steep transition from the intake pipe to the sac volume causes a strong flow recirculation in the sac. Lastly, shear cavitation cannot develop along the complete hole due to its conicity and it vanishes at almost one third of the hole. Injectors ID-3 and ID-10 show very similar behavior in terms of shear cavitation. With such a moderate development of shear cavitation, the position of the strings of fuel-vapor can be quite easily distinguished by the shadowgraph pictures. This is especially useful because a large amount of string cavitation develops in the nozzle. String cavitation appears visually as vertical filaments. They can appear as a single full ligament, covering all the hole length. They can also appear partly at the hole entrance, at the hole end or in both (see Fig. 4 and 5). Ligaments mostly appear as vertical strings but some slight bending can be visible. String cavitation is more visible than shear cavitation in the geometries studied. This is a surprising result that

will be discussed in detail in the next sections. Additionally, in configuration ID-10, string cavitation is more intense than in ID-3. This is a consequence of the flow conditions at the hole entrance (due to the sac geometry) and of the hole geometry and it will be also discussed in the next sections.

It can be stated that simulations are reproducing with a very satisfying agreement the typical appearance either of shear and string cavitation. The LES-VOF solver [28] is able to capture the large, coherent eddies to reproduce accurately the complex features of the two phase flow, at least for the two studied cases. The fine-mesh is adapted to reproduce the asymmetry and small details of the shear cavitation zone and the cavitating vortex core. Despite the large grid used, space filtering used certainly cannot properly describe the thinnest vortex cavitating cores.

6. Flow Analysis

The agreement achieved between simulations and experimental visualizations allows us to consider the simulation reliable enough to be used for the in-nozzle multiphase flow analysis. The main features of the flow pattern in the geometries studied are summarized in the sketch of Fig. 7: the flow pattern presents two secondary vortices on the sides, that turn into two three-dimensional counter-rotating vortical structures centered in the nozzle axis. Only after entering into the nozzle, the rotation axis of these vortical structures tends to align with the nozzle axis.

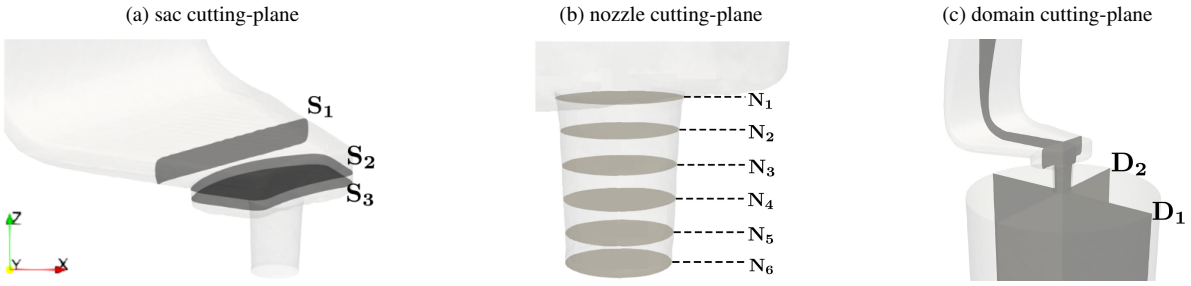

Figure 6: The flow analysis is based on time- and space- averaged flow quantities over: a) the three cross sections $\mathbf{S_1}$, $\mathbf{S_2}$ and $\mathbf{S_3}$ located in the sac; b) cross-planes $\mathbf{N_i}$, i$\in$ [1; 6] along the nozzle; c) two cutting planes, $\mathbf{D_1}$ (lateral) and $\mathbf{D_2}$ (frontal), parallel to the nozzle axis are defined by the θ_1=0^o and θ_2=90^o respectively.

The study presented in this paper aims at providing a detailed characterization of the in-nozzle flow field, to study the influence of the sac geometry on the formation of shear and vortex cavitation. A qualitative comparison of numerical and experimental visualizations for the two configurations, is used for validation and it is shown first. Then, a deep analysis of the in-nozzle flow features is presented and it is organized as follows:

1) *study of the influence of the feeding system/nozzle sac on the flow field at the nozzle entrance*. Flow features in the sac volume are studied; additionally, the fuel distribution at the nozzle inlet section for the two configurations investigated are studied, to identify the regions where the flow detachment and the largest recirculation occurs (Sec. 6.1);

2) *study of the internal nozzle flow field and evolution of the shear and string cavitation*. Time-averaged velocity magnitude, static pressure, liquid volume fraction and nozzle-streamwise vorticity are plotted in the nozzle to identify the cavitating regions of the flow; they are used to visualize the counter-rotating vortical structures and secondary vortices in the nozzle, their intensity and direction of rotation and how they radially expand (see Sec. 7).

3) computation of the *time-averaged values of nozzle coefficients* (Sec. 8) and an unsteady flow analysis is presented in Sec. 9.

The flow analysis is based on time- and space- averaged flow quantities over several cross planes, namely: a) the three cross sections S_1, S_2 and S_3 located in the sac, Fig. 6a; b) six cross-planes in the nozzle, referred as to $N_1 - N_6$ (Fig. 6b); c) two cutting planes, that will be referred in the following as to D_1 and D_2 (see Fig. 6c).

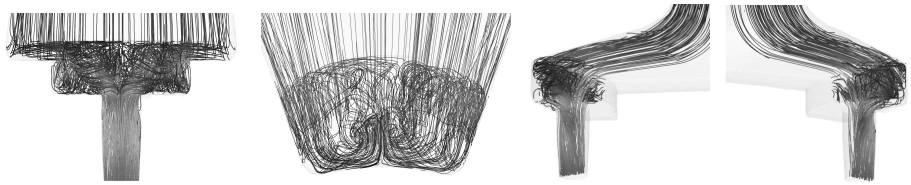

(a) Front view (b) Top View (c) Left half view (d) Right half view

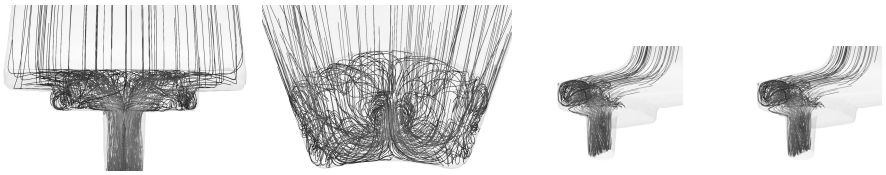

(e) Front view (f) Top View (g) Left half view (h) Right half view

Figure 7: Three-dimensional representation of the average streamlines for injector configuration ID-3 (a-d) and ID-10 (e-h).

6.1. Influence of the feeding system/nozzle sac on the flow field at the nozzle entrance

Fig. 8 and Fig. 9 show the contour plots describing the main features of the flow field on planes S_1, S_2 and S_3 of Fig. 6c for injectors ID-3 and ID-10 respectively. Differences in the velocity field between the two configurations, in terms of mean value and fluctuations, are a consequence of the different geometry of the feeding system and in the lift (see Fig. 1). While entering into the sac, the flow then separates and a recirculating region forms, as apparent by plane S_2 (Figs. 8 and 9, d-f). This region is wider for configuration ID-10 and becomes larger at the nozzle inlet section (plane S_3, Figs. 8 and 9, g-i), where the velocity profile is almost symmetric. Differences in the average flow velocity and in the flow-symmetry in section S_1 are responsible of the different vortical structures evidenced on planes S_2 and S_3 for the two injector configurations. Flow separation is visible on plane $\mathbf{S_2}$ (Fig. 8 and 9, d-f): two small vortices appear on the side walls and they are also present in both configurations on plane $\mathbf{S_3}$. The intensity of the flow separation can qualitatively be estimated by observing the different extension of the side vortices. In both cases, the largest average flow velocity is located near the nozzle entrance, as also evidenced by the two-dimensional streamlines in Fig. 8g-i and 9g-i. It is interesting to observe that in configuration ID-3, the average flow velocity and fluctuations are spread over a larger area on sections $\mathbf{S_2}$ and $\mathbf{S_3}$; this is most probably due to the shorter volume of the dead space and of the nozzle, that favors a reverse flow that interacts with the central counter rotating vortices. Fig. 10 and 11 show the contour plots of the velocity flow field on planes $\mathbf{D_1}$ (a-c) and $\mathbf{D_2}$ (d-f); for both injectors, the reverse flow generated from the recirculation in the dead zone of the sac limits the extension of the recirculating zone from the step, as clearly confirmed by contour plots on plane $\mathbf{D_1}$. The visualizations show that flow features are similar for the two injectors in the flow sac and at the nozzle entrance; on the other hand the flow field for the two injectors is very different in the nozzle, as apparent in Figs. 10 and 11.

	Plane S_1		Plane S_2		Plane S_3	
Config.	ID-10	ID-3	ID-10	ID-3	ID-10	ID-3
$< \overline{\mathbf{U}} > [m/s]$	56.64	43.05	27.53	15.34	19.29	15.45

Table 3: area-weighted average of $< \mathbf{U} >$ for plane S_1, S_2 and S_3.

To summarize, different sac geometries of the two injectors provide very similar flow distributions at the nozzle entrance and comparable average velocity in sections S_2 and S_3, as shown in Tab. 3. On the other hand, the flow atomization of the two injector configurations at the nozzle outlets is very different: a possible reason for this might be a different amount of cavitation for the two nozzle configurations. The following analysis is focused to a more quantitative estimation of these statements.

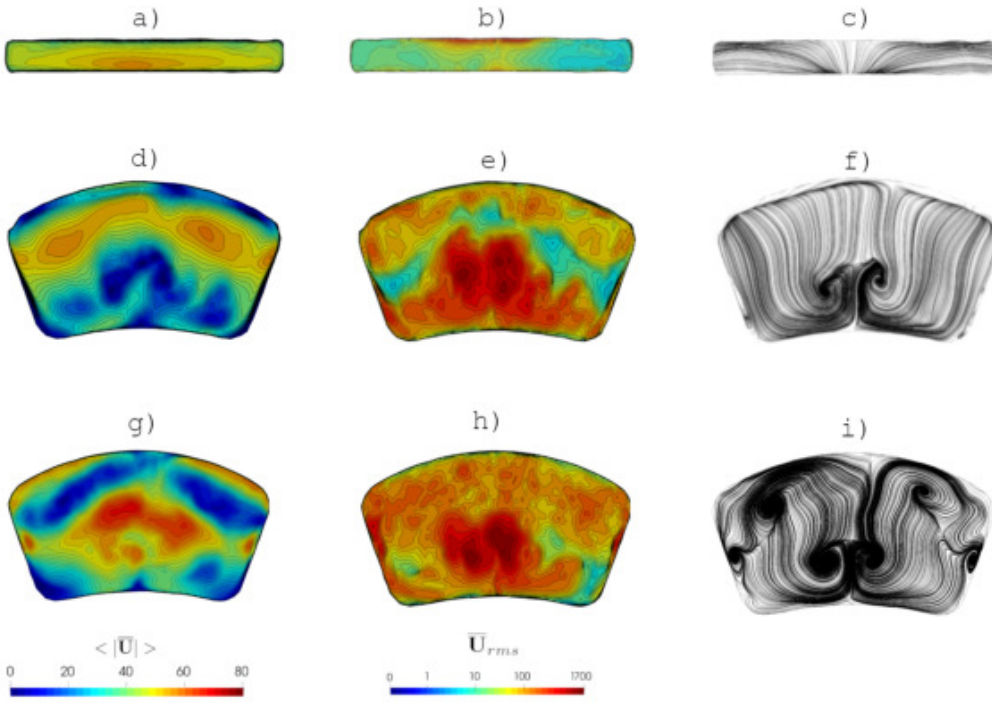

Figure 8: flow analysis on planes $\mathbf{S_i}$ (i=1,..3) of Fig. 6 for injector ID-3: plane $\mathbf{S_1}$ (a-c), plane $\mathbf{S_2}$ (d-f) and plane $\mathbf{S_3}$ (g-i). Time-averaged mean flow velocity (a,d,g); time-average velocity fluctuations (b,e,h); velocity streamlines (c,f,i).

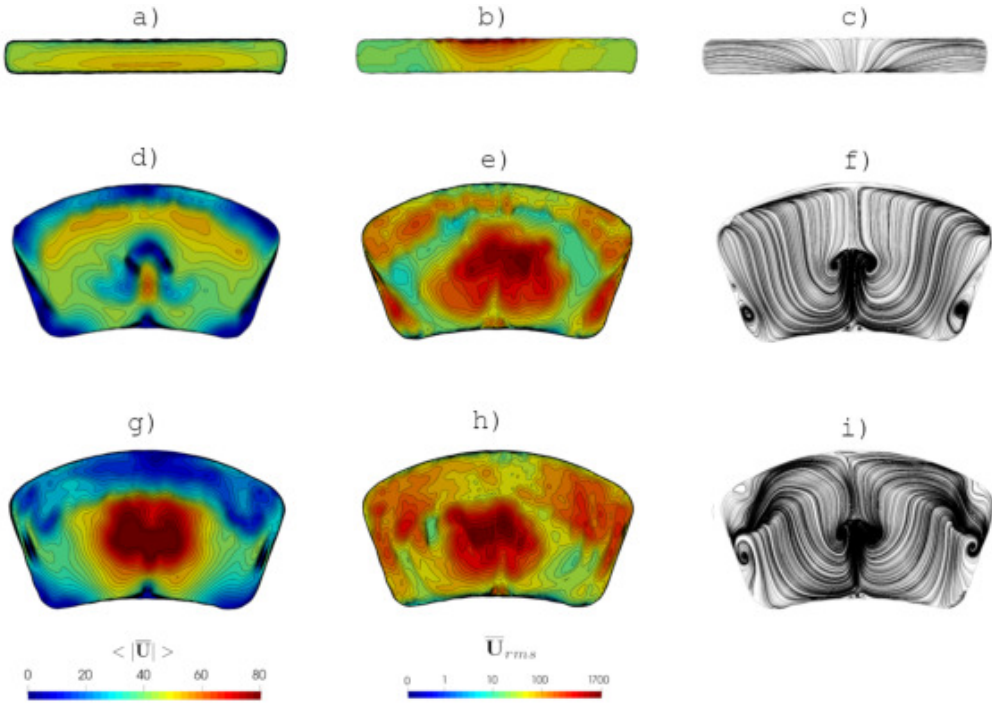

Figure 9: flow analysis on planes $\mathbf{S_i}$ (i=1,..3) of Fig. 6 for injector ID-10: plane $\mathbf{S_1}$ (a-c), plane $\mathbf{S_2}$ (d-f) and plane $\mathbf{S_3}$ (g-i). Time-averaged mean flow velocity (a,d,g); time-average velocity fluctuations (b,e,h); velocity streamlines (c,f,i).

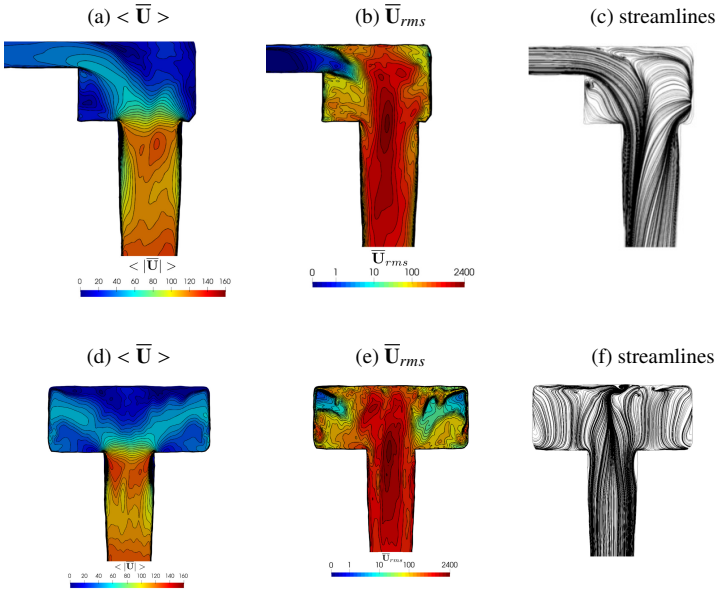

Figure 10: Configuration ID-3: velocity flow field on planes $\mathbf{D_1}$ (a-c) and $\mathbf{D_2}$ (d-f).

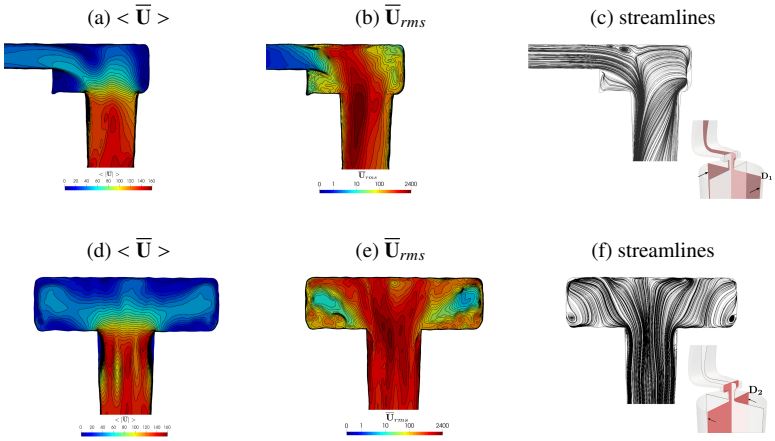

Figure 11: Configuration ID-10: velocity flow field on planes $\mathbf{D_1}$ (a-c) and $\mathbf{D_2}$ (d-f).

7. In-nozzle flow field

A main goal of this research is to identify the mechanisms driving to very different flow atomization in the two injector nozzles. The two injectors studied operate at the same injection pressure and very similar Mass Flow Rate (MFR), see Fig. 20. The volume of the region where flow recirculation occurs is not very different among the two geometries. Also the sector angle is the same. They present different sac heights and hole–to–step distances (named here offs-H) though, while the fuel pattern in the injector sac volume does now show relevant differences in the flow features, as seen in Figs. 7, 8, 9, 10 and 11. Also the flow pattern at the hole entrance is very similar. The pattern of the primary flow coming from the inlet channel separates while it encounters a step and it immediately turns to enter into the hole. Similarly to the Backward Facing Step (BFS), where the flow characteristics can be linked to its aspect ratio, it is here proposed a ratio r to characterize the separating flow in the sac of the injector, defined as:

$$r = \frac{\text{lift} + \text{H}}{\text{off-H}} \tag{11}$$

The discrepancy between the values of r calculated for ID-3 and ID-10 lies in a range of 5%: from (11), r= 2.12 for ID-3, while r= 2 for ID-10.

We focus then our attention: a) on the study of the formation of vortices at the hole entrance (plane $\mathbf{N_1}$); b) on the analysis of the evolution of the in-nozzle flow, by the information provided by the validated high-fidelity simulations. Two parameters are identified as possible promoters for the formation of string vortices at the hole entrance: the development of the streamwise vorticity and the amount of the tangential flow velocity on plane $\mathbf{N_1}$, as shown in Fig. 12. For each cell of plane $\mathbf{N_1}$ with reference to Fig. 12, the flow is labelled as *side flow* ($|\overline{U_z}| > |\overline{U_x}|$), *direct flow* ($|\overline{U_x}| > |\overline{U_z}| \cap \overline{U_x} > 0$) and *reverse flow* ($|\overline{U_x}| > |\overline{U_z}| \cap \overline{U_x} < 0$).

(a) injector ID-3

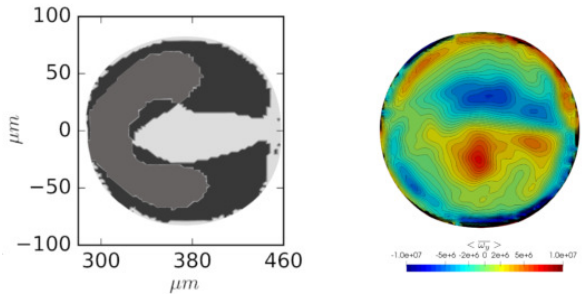

(b) injector ID-10

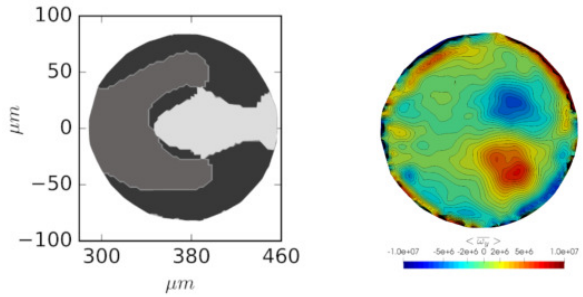

Figure 12: flow features on plane $\mathbf{N_1}$ for injector configurations ID-3 and ID-10. Left: ■ direct flow ■ side flow ■ reverse flow. Right: time-averaged flow vorticity.

Results for the two injector configurations studied are reported in Fig. 12 and in Tab. 4. For both injectors, the percentage of cells where the side, reverse and direct flow on section N_1 is very similar. Also, the area magnitude, the average mass-flow rate (MFR) and the average velocity on the plane N_1 for the two injectors do not differ significantly.

	ID-3			ID-10		
	side	direct	reverse	side	direct	reverse
Area [%]	44.5	35.8	19.7	43.9	33.3	23.8
MFR [g/s]	0.66	0.6	0.3	0.682	0.59	0.31
$< \overline{\mathbf{U}} >$ [m/s]	99.5	113.3	103.9	100.3	118.5	84.8

Table 4: percentage of the area of plane $\mathbf{N_1}$, velocity magnitude and mass-flow rate (MFR) of different types of flows: side/direct/reverse.

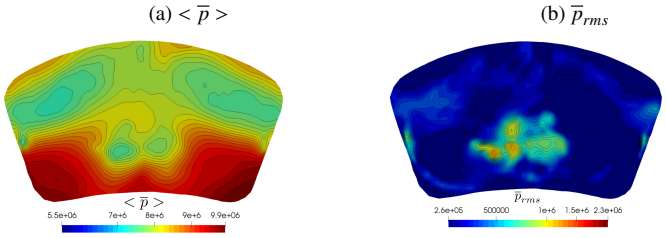

Figure 13: injector ID-3, plane $\mathbf{S_3}$ of Fig. 6. Pressure field (a) and pressure RMS (b). Quantities are time-averaged.

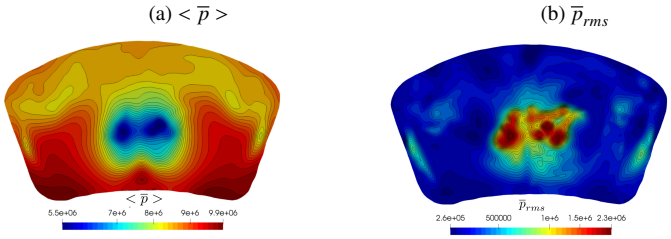

Figure 14: injector ID-10, plane $\mathbf{S_3}$ of Fig. 6. Pressure field (a) and pressure RMS (b). Quantities are time-averaged.

Besides, the contour plot of the time-averaged vorticity on plane $\mathbf{N_1}$ evidences some difference in the vortex structures at the entrance of the hole; these differences are not sufficiently large to identify the sac geometry as a main driver of the different flow cavitation along the nozzle and, eventually, of the different spray atomization at the nozzle outlet. The same holds for the average pressure level in the sac, as reported in Figs. 13, Fig. 14 and in Tab. 5).

It can be therefore concluded that the different geometry of the sac in the two injectors is not the main driver for the flow atomization at the nozzle exit.

	plane S_1		plane S_2		plane S_3	
	ID-10	ID-3	ID-10	ID-3	ID-10	ID-3
$< \overline{p} >$ [bar]	91.31	91.16	87.53	87.18	85.69	83.27

Table 5: area-weighted average of $< \overline{p} >$ for plane S_1, S_2 and S_3

Since the nozzle inlet and outlet diameters are the same for the two injectors, it is reasonable to think that different flow features in the injectors are driven by the nozzle length and this, in turn, has an impact on the pressure field inside the nozzles. The pressure drop over the nozzle is the same for the two injectors, since it is forced by the boundary conditions: liquid pressure is 100 bar at the inlet and the reservoir where the fuel is injected is at ambient pressure. This is apparent from Figs. 15 and 16, where the average pressure field and the fluctuations in pressure are reported for planes $\mathbf{D_1}$ and $\mathbf{D_2}$ of Fig. 6. Besides, different nozzle lengths affect the capability of the flow to reorganize.

(a) $< \overline{p} >$

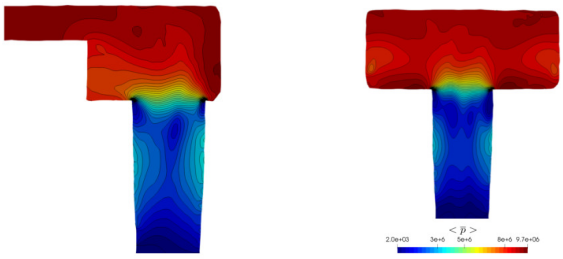

(b) $\overline{p}_{rms}$

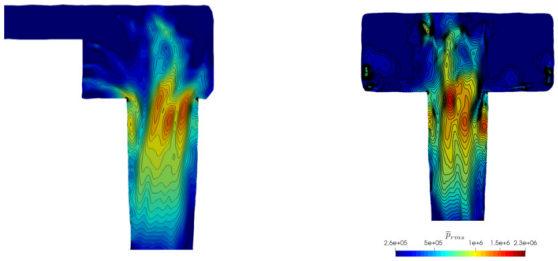

Figure 15: injector ID-3: a) time-averaged pressure field $< \overline{p} >$; b) time-averaged pressure rms $\overline{p}_{rms}$ on sections $\mathbf{D_1}$ (left) and $\mathbf{D_2}$ (right) of Fig. 6.

(a) $< \overline{p} >$

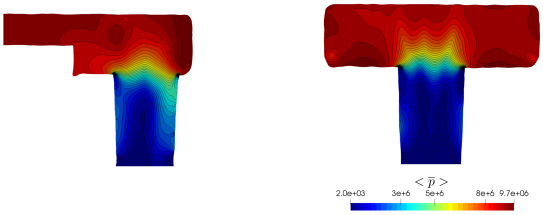

(b) $\overline{p}_{rms}$

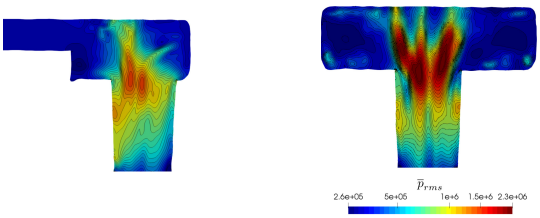

Figure 16: injector ID-10: a) time-averaged pressure field $< \overline{p} >$; b) time-averaged pressure rms $\overline{p}_{rms}$ on sections $\mathbf{D_1}$ (left) and $\mathbf{D_2}$ (right) of Fig. 6.

Pressure losses occur at the nozzle entrance; there, a recirculating region forms and shear cavition is observed while a vortex core also generates. From the time-averaged pressure field in Figs. 13, 14, 15a and 16a, it is not possible to detect the appearance of cavitating strings in the nozzle. Being the string cavitation a very seldom and random phenomenon, it might be canceled by the time-averaging procedure. Therefore, the appearance of cavitating strings is detected by looking at high pressure fluctuations in the nozzle, Figs. 15b and 16b. In regions where the intensity of pressure fluctuations is of the same order of magnitude of the mean flow pressure, string cavitation might occur. In Figs. 13 and 14, the flow pressure significantly deviates from the average condition; since vortices are not

stable within the sac but they periodically grow and disrupt, those strings represent spots where string cavitation is likely to occur (see also Figs. 4 and 5 for comparison). Being strings stretched over the nozzle, the L/D ratio and the conicity factor K_g are of foremost importance to influence the evolution of the pressure field in the nozzle.

It is important to mention that the three-phase solver does not detect any presence of air in the hole at the mentioned operating conditions for the two injector configuration, as also confirmed in [29].

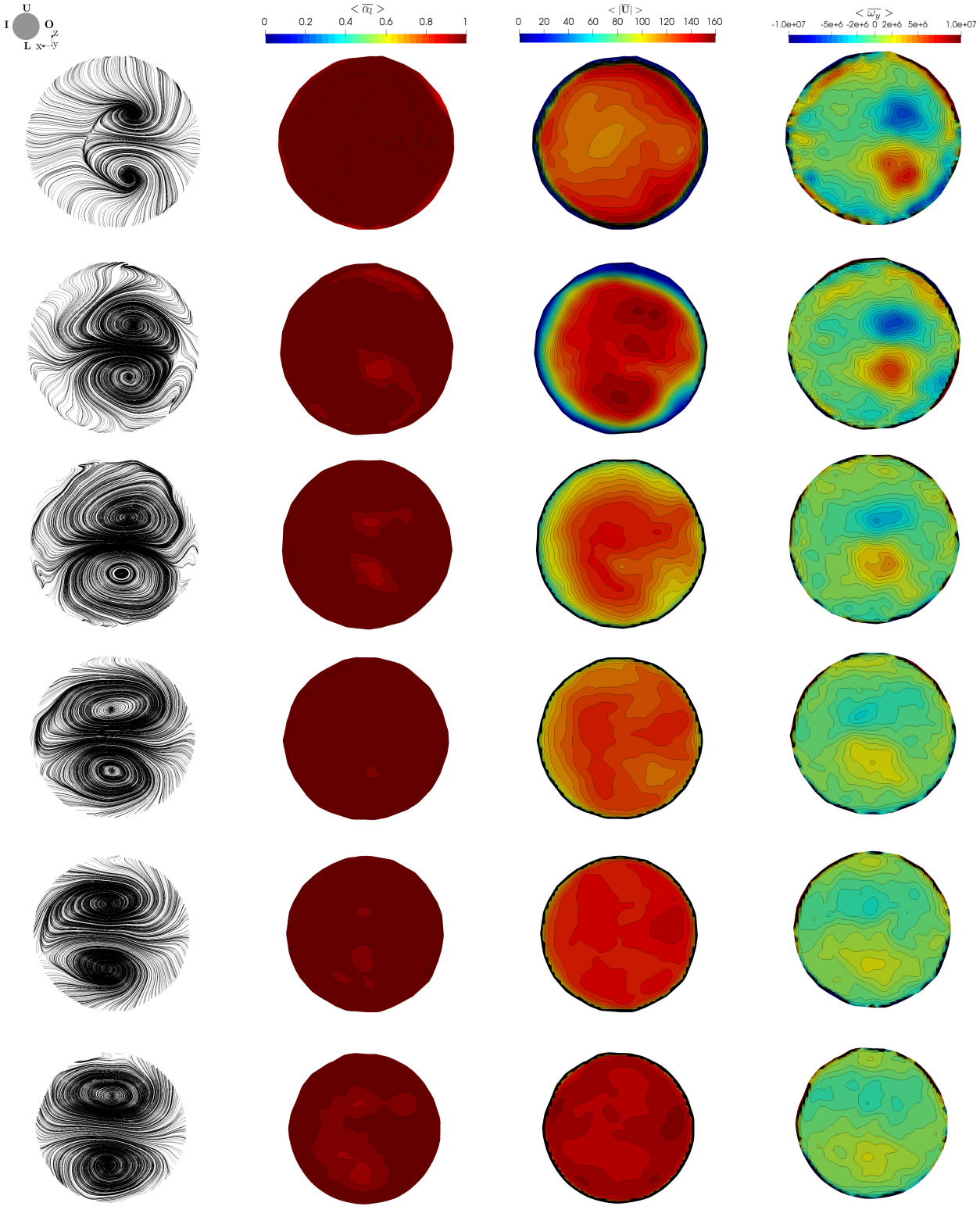

(a) average streamlines (b) $< \overline{\alpha_l} >$ (c) $< |\overline{\mathbf{U}}| >$ (d) $< \overline{\omega_y} >$

Figure 17: injector ID-3: average quantities on nozzle cutting planes N_1, N_2, N_3, N_4, N_5, N_6 (from top to bottom).

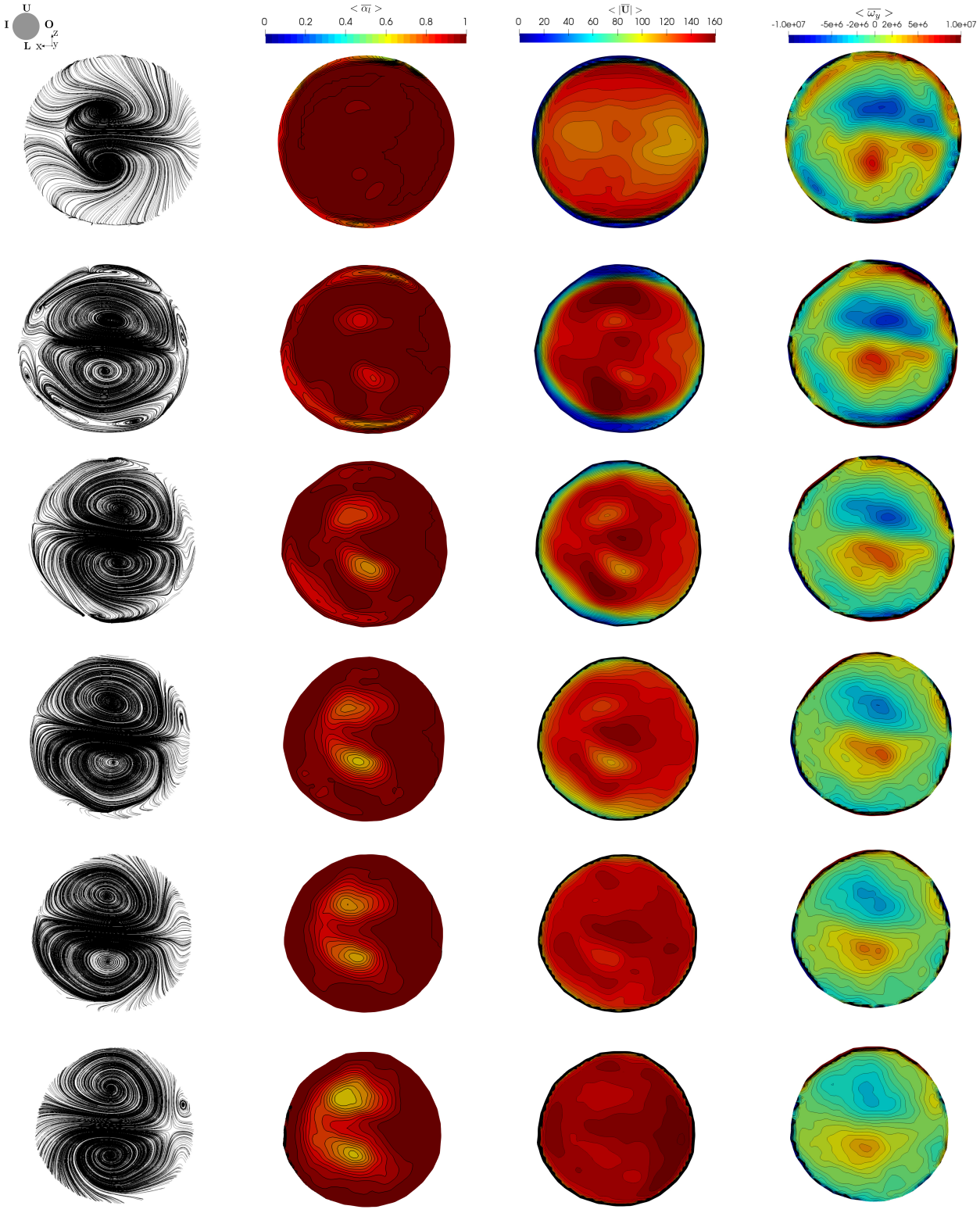

(a) average streamlines (b) < $\overline{\alpha_l}$ > (c) < $|\overline{\mathbf{U}}|$ > (d) < $\overline{\omega_y}$ >

Figure 18: injector ID-10: average quantities on nozzle cutting planes N_1, N_2, N_3, N_4, N_5, N_6 (from top to bottom).

In Fig. 17b and 18b, the time-averaged liquid fraction over planes N_1 to N_6 is shown. Near the nozzle wall of injector ID-3 (Fig. 17b), the flow from the sac detaches and shear cavitation appears in a recirculating low-pressure region. On plane N_4, the flow is fully reattached, as evidenced by the streamlines (Fig. 17a). At the center of the nozzle hole, the countour plots of the vorticity (Fig. 17d), of the streamlines (Fig. 17a) and of the flow velocity (Fig. 17c) highlight the formation of a small amount of fuel vapor at the hole center on plane $\mathbf{N_3}$, where two counter-rotating vortices appear. The large average flow pressure, maintained in ID-3 over the short length of the nozzle (Fig. 19d), avoids a strong vortex cavitation and, consequently, a strong atomization of the flow.

Also in injector ID-10 (Fig. 17), shear cavitation is triggered by the flow detachment near the nozzle walls on planes $\mathbf{N_2}$ and $\mathbf{N_3}$ (Fig. 18b). On planes $\mathbf{N_4}$, $\mathbf{N_5}$ and $\mathbf{N_6}$ string cavitation progressively becomes stronger; besides, cavitating vortices favors a faster flow reattachment at the walls. As a consequence, the flow velocity in injector ID-10 is larger and the average pressure is lower (Fig. 18c), if compared to injector ID-3. The resulting stronger amount of cavitation causes the stronger atomization of the flow.

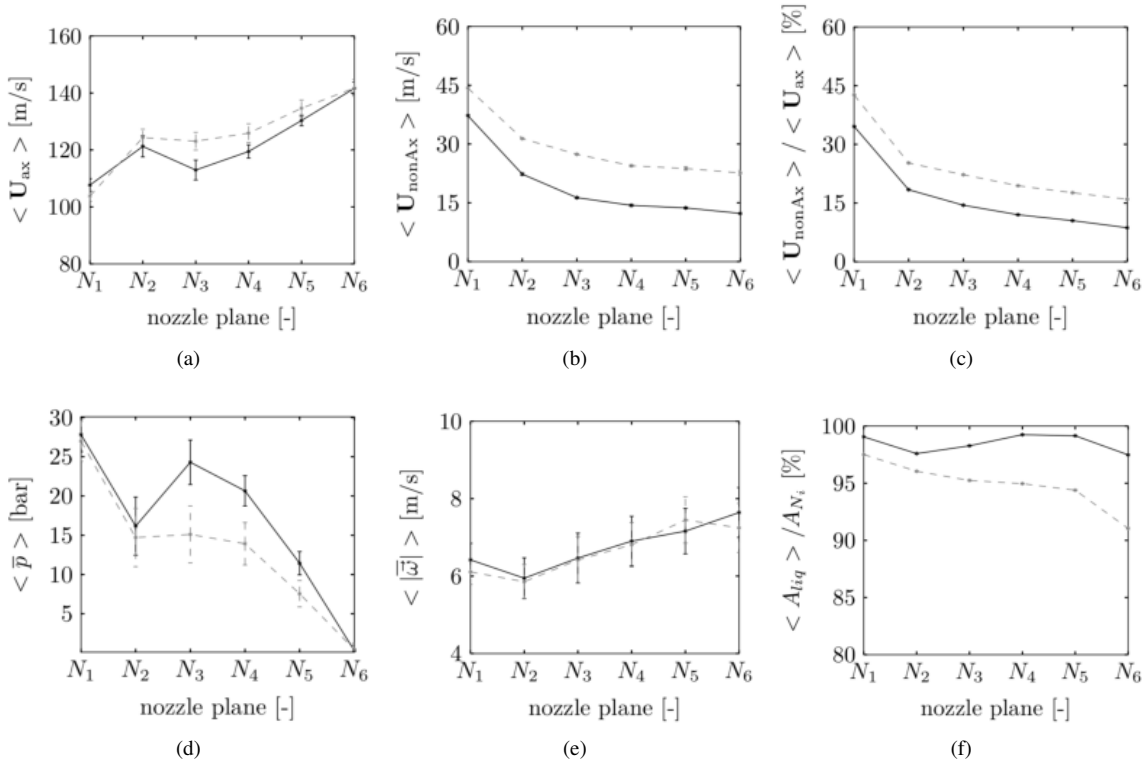

Figure 19: Mean values over the nozzle axis, on planes N_1 to N_6, of time-averaged quantities: 1) MFR-weighted average axial velocity; b) magnitude of the MFR-weighted average non-axial velocity; c) radial/axial velocity ratio; d) average pressure; e) MFR-weighted vorticity magnitude; f) liquid area over cross sectional area. Legend: — ID-3; - - ID-10.

In Fig. 19a, a comparison between the two injectors is carried out by looking at the main features of the flow in the nozzle holes. Quantities over six equispaced parallel planes in the nozzle holes ($\mathbf{N_1}$-$\mathbf{N_6}$ of Fig. 6) are plotted. The position of each plane is normalized by the length of the nozzle. From Figs. 19a, it is apparent that the axial component of the flow velocity is progressively increasing over the injector nozzles. This is a direct consequence of the combined effect of the nozzle conicity K_g and of the cavitation. Swirling vortices generated at the nozzle entrance expand and progressively disappear in proximity of the nozzle end (planes $\mathbf{N_4} - \mathbf{N_6}$); the magnitude of the non-axial velocity therefore reduces (Fig. 19b) and the axial velocity progressively increases (Fig. 19a), so that the ratio among the two quantities is decreasing (Fig. 19c). Because of the acceleration of the flow in the hole (Fig. 19a), shear cavitation tends to disappear. The larger non-axial velocity in injector ID-10 (see Fig. 19b) favors a stronger string cavitation. This is also confirmed by Fig. 19f. The corresponding time-averaged mean pressure over planes $\mathbf{N_1}$-$\mathbf{N_6}$ is shown in Fig. 19d. As expected, time-averaged pressures on planes $\mathbf{N_1}$ and $\mathbf{N_6}$ are the same, being forced by the boundary conditions. A stronger pressure recovery to the atmospheric pressure is noticed for ID-10 near the nozzle

exit, between planes $\mathbf{N_5}$ and $\mathbf{N_6}$. The larger conicity factor k_{geom} of injector ID-3 favors a pressure recovery of almost the 85% of the nozzle average inlet pressure, with a local maximum at plane N_3. The longer hole of injector ID-3 allows for the formation of larger detachment regions at the nozzle entrance and favors a different intensity of swirl cavitation. The vorticity magnitude (Fig. 19e) has a similar trend in the two configurations, but ID-3 shows a stronger decay while the flow is reaching the nozzle end. Also, the liquid area of the flow on the different nozzle sections $\mathbf{N_1} - \mathbf{N_6}$ (Fig. 19f) is larger for injector ID-3, as a consequence of a weaker cavitation of the liquid along the nozzle. The higher conicity of injector ID-3 results in a lower atomization of the liquid, that fills most of the nozzle area on sections $\mathbf{N_3} - \mathbf{N_6}$.

8. Discharge coefficient

Fig. 20 shows the variation in time of some relevant parameters for the injectors ID-3 and ID-10 at the nozzle outlet (plane N_6), namely: the discharge coefficient C_d, the velocity coefficient C_v, the area coefficient C_a and the liquid void fraction α_l. The discharge coefficient C_d of the injectors is computed as:

$$C_d = \frac{< \dot{m} >}{\dot{m}_{th}} = \frac{A_{\text{eff}}}{A_{th}} \frac{U_{\text{eff}}}{U_{th}} \frac{\rho_l}{\rho_l} = C_a C_v \tag{12}$$

where A_{th} and A_{eff} is the real geometric cross sectional area of plane N_6, ρ_l is the density of the liquid fuel and $< \dot{m} >$ is the average mass flow rate from the simulation, $\dot{m}_{th}$ is the mass flow rate calculated using the velocity from the Bernoulli theorem:

$$U_{th} = \sqrt{\frac{2(p_{inj} - p_{back})}{\rho_l}} \tag{13}$$

From Eq. (12), C_d is calculated as the product of two coefficients:

- the velocity coefficient C_v, defined as the ratio between the actual and the ideal velocity, calculated by the Bernoulli's theorem (see Eq. 13):

$$C_v = \frac{U_{\text{eff}}}{U_{th}} \tag{14}$$

  where U_{eff} is computed using the normal area average:

$$\frac{\sum_{j=1}^{k} < \overline{\mathbf{U}}_j > \cdot \mathbf{S_f}_{,j}}{\sum_{j=1}^{k} |\mathbf{S_f}_{,j}|} \tag{15}$$

  In Eq. (15), k is the number of cell faces that are used for the discretization of the plane where the spatial average is computed; $< \overline{\mathbf{U}}_j >$ is the time-averaged velocity on the *j-th* face, $\mathbf{S_f}_j$ is the surface area vector of the j-th face computed as $|\mathbf{S_f}_j| \cdot \hat{\mathbf{n}}_j$ where $\hat{\mathbf{n}}_j$ is the unity normal vector to the j-th face of the surface;

- the area coefficient C_a:

$$C_a = \frac{A_{\text{eff}}}{A_{th}} \tag{16}$$

  is defined as the ratio between effective area to the geometrical area, measured by XCT, being:

$$A_{\text{eff}} = \sum_{j=1}^{k} |\mathbf{S_f}_{,j}|_{(<\overline{\mathbf{U}}>_j \cdot \hat{\mathbf{n}}_j > 0) \cap (<\overline{\alpha_l}>_j = 1)} \tag{17}$$

  In Eq. (17), the condition $(< \overline{\mathbf{U}} >_j \cdot \hat{\mathbf{n}}_j) > 0$ ensures to compute the effective area on the basis of the liquid leaving the nozzle ($< \overline{\alpha_l} >_j = 1$).

Density variations in the nozzle due to phase-change are taken into account by C_d and C_v (together with C_a, they are listed in Tab. 8). Oscillations in the C_a are mostly linked to changes of α_l (Fig. 20): the presence of vapor at the outlet reduces the available area to inject liquid fuel, Figs. 10 and 11; additionally, it is also responsible for oscillations in the mass flow rate.

	ID-3	ID-10
C_d	0.79048	0.74705
C_a	0.93162	0.9077
C_v	0.84847	0.823

Table 6: Values of the coefficients C_d, C_a and C_v from the numerical simulations for injector ID-3 and ID-10. Time averaging starts after t= 110 μs, when the influence of the initial conditions on the solution is assumed to be negligible.

The discharge coefficient is therefore influenced by the ratio between the fuel-vapor and the liquid. Pressure losses in the sac and at nozzle entrance (plane $\mathbf{N_1}$) also influence the discharge coefficient, but those are not linked to the amount of phase change. The shorter nozzle length of injector ID-3 favors a higher recovery of the initial kinetic energy, as apparent from its values of C_d and C_v. The flow detachment for this configuration does not extend to the outlet section (plane N_6), while the convergent nozzle geometry contributes to recover a part of initial kinetic energy. The rate of the kinetic energy between planes N_3 and N_6 the is larger for ID-3 than for ID-10, as reported in Fig. 19a.

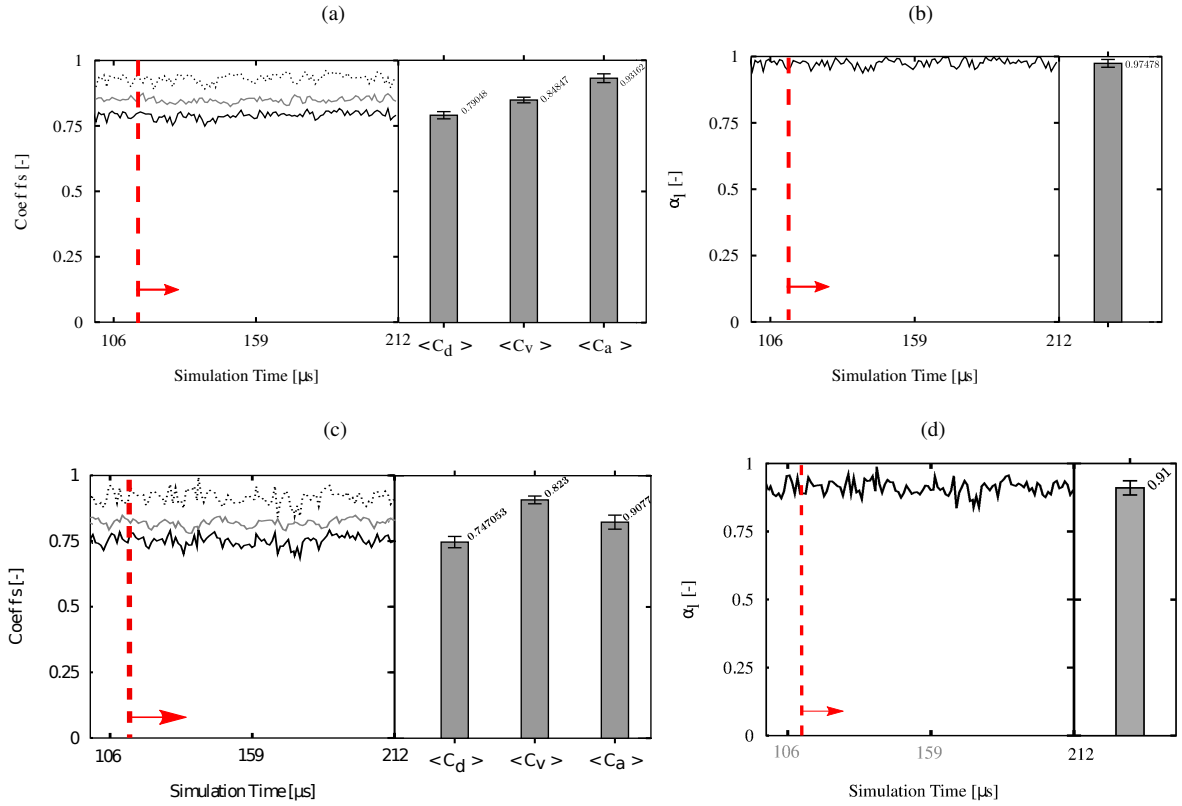

Figure 20: Evolution in time and time-averaged of of C_d, C_v, C_a and of the area-weighted liquid fraction on plane N_6 for ID-3 (a, b) and ID-10 (c, d). Time averaging is performed on a time interval of 80 μs of the simulation, starting from t= 132 μs. Legend: a, c) – C_d; - - - C_v; — C_a; b, d) — area-weighted liquid fraction.

9. Unsteady vortex flow physics and behavior

An analysis of the unsteady vortex flow physics in the nozzle is presented for configuration ID-10, because it exhibits a stronger cavitation with respect to configuration ID-3. Starting from t= 117 μs (red dashed line, Fig. 20), forty-one snapshots (Figs. 23 and Fig. 22) in a time interval of 90 μs of the simulation were analyzed, corresponding to two flow-through times of the hole. For each snapshot, the nature of the newly generated amount of fuel vapor in the volume was observed and it was classified as follows: a) if the fuel vapor was found near the walls, in a recirculating region or along the nozzle axis, then its origin was attributed to the shear cavitation; b) if the new fuel-vapor was

found far from the walls and it was included in a swirling vortex, then its origin was attributed to string cavitation. The criterion mentioned above has been applied to each snapshot to characterize the cavitation in the nozzle and populate the plots of Fig. 21.

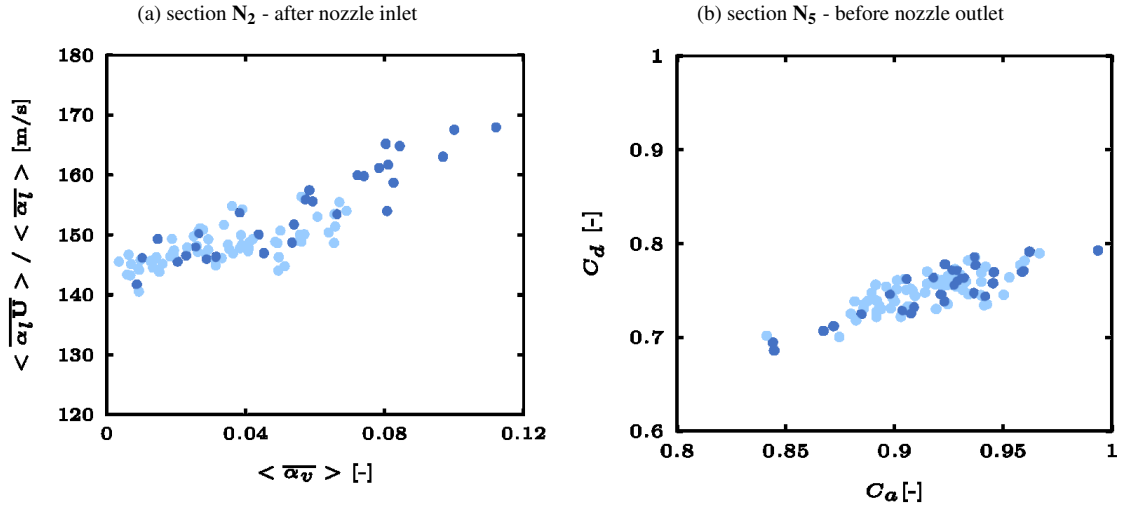

Figure 21: global characterization of the unsteady behavior of the flow at planes N_2 and N_5 of Fig. 6a; a) conditional liquid average velocity versus vapor fraction; b) area coefficient versus flow coefficient. ● events with shear; ● events without shear.

Shear cavitation is produced at the liquid shear layer forming at the hole entrance; the rate of vaporization can be controlled by the modification of the orifice design, which influences the pressure recovery. An alternative way to study this effect is to link the instantaneous flow velocity in the nozzle at a certain plane with the fuel-vapor void fraction α_v, that is proportional to the rate of vaporization. It is important to note that with a single-fluid solver [28], the liquid velocity $< \overline{\alpha_l \mathbf{U}} > / < \overline{\alpha_l} >$ can only be estimated; this is done by weighting the time-averaged flow velocity by the liquid void fraction (see y-axis, Fig. 21a). The liquid velocity increases with the amount of vapor, since the effective flow area on the nozzle cross plane of the liquid reduces. Fig. 21a confirms that string cavitation appears when a large amount of fuel vapor in the hole is combined with large velocity of the liquid. In Fig. 21b, the correlation of the flow coefficient C_d with the effective flow area (through the C_a coefficient) is shown. The spreading of the points around a theoretical linear relationship between C_a and C_d suggests that the value of C_v in Eq. (12) varies from time to time. This is assumed to be a consequence of the flow detachment at the nozzle entrance, of the chaotic behavior of the flow and to the presence of a secondary flow that can cavitate. It is finally important to note that the relationship between C_a and C_d is independent on the type of cavitation.

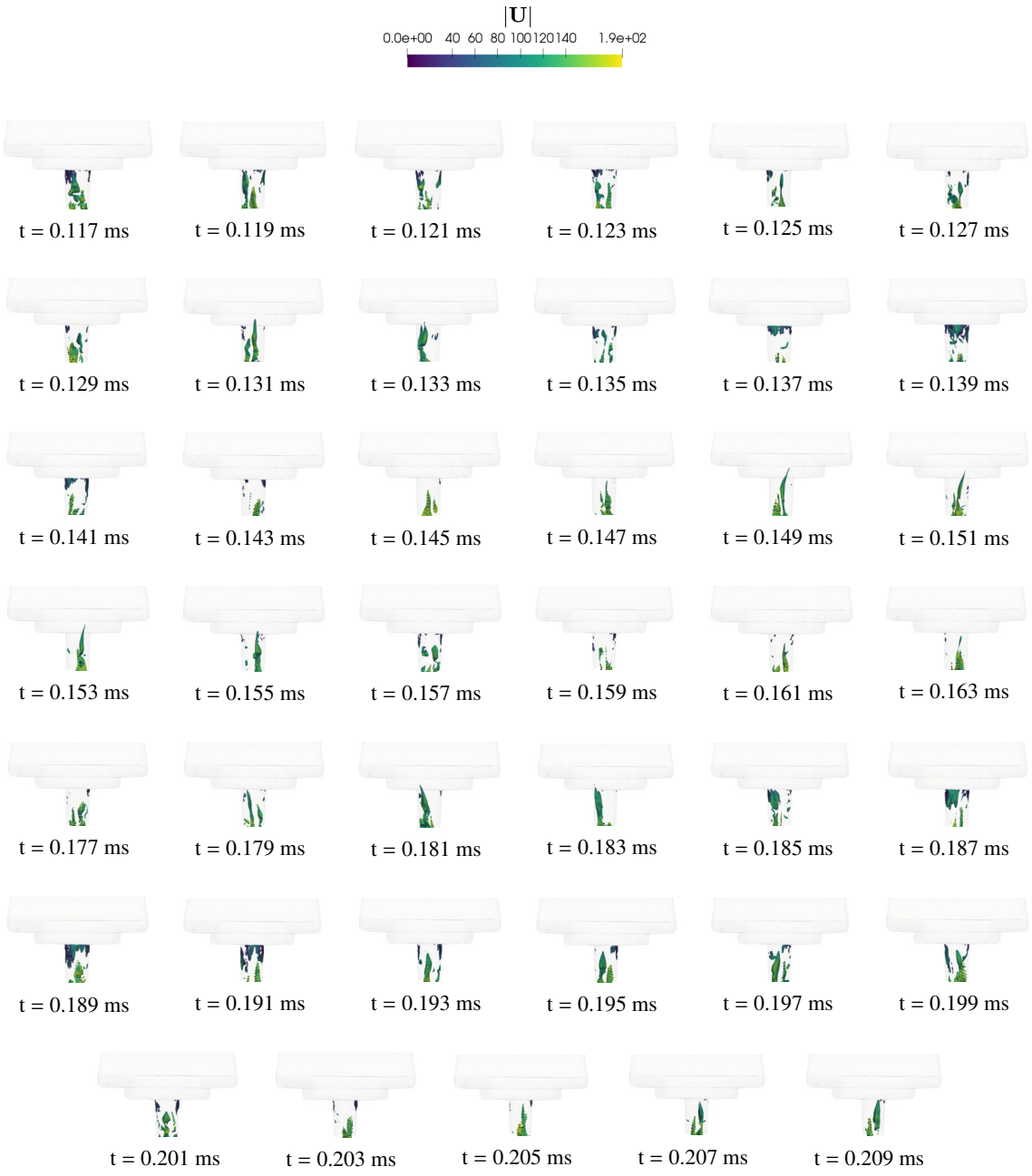

Figure 22: Instantaneous isosurfaces α_v=0.3 showing the evolution of the vapor pockets generated by string and shear cavitation into the nozzle of injector configuration ID-10 during the injection event.

Figure 23: Isosurfaces of the second invariant of the rate of deformation tensor (Q-criterion), showing the evolution of the vortex strings into the nozzle of injector configuration ID-10 during cavitation.

Figures 22 and 23 are representative of the evolution of the cavitation in the nozzle (enlarged pictures are provided in additional online material).. A counter-rotating vortex pair associated with the jet cross-section evolves along the convergent nozzle, the flow accelerates, the pressure decreases (see Fig. 19d) and the liquid progressively cavitates. Cavitating pockets of fluid expands radially in the vortexes. This is also observed experimentally. At the Reynolds numbers considered, a counter-rotating vortex pair is typically unstable. Flow unsteadiness and vortex pair instabilities make the vortex pair merge or brake in multiple eddies. The counter-rotating vortex pair may appear with a symmetric or asymmetric shape. Finally, during its evolution, the vortex pair can move towards the nozzle walls. Then, shear cavitation appears, see t $\in [169, 175]\,\mu$s. Shear-cavitation can stabilize in a specific region at the hole entrance, where the side flow is intense (see Fig. 12). Typically, shear cavitation is weak and localized in small volumes; more rarely, shear cavitation can uniformly develop at the hole inlet edge (see t $\in [137, 139]\,\mu$s or on a part of it. As the recirculating vortex pair reappears, $t \in [199, 207]\,\mu$s, shear cavitation is no longer observed. The primary flow coming from the inlet channel and turning inside the sac volume adapts to the injector geometry, favoring a progressive deviation before the hole entrance (see Figs 9 and 14). The primary flow strongly interacts in the sac with the flow labelled in Fig. 12 as "reverse". As a result, a swirling vortex pair is generated and most of the mass flow in the nozzle axial direction is found on the side (see side flow in Fig. 12), that is also the preferred location of shear cavitation spots. To summarize, the string cavitation regime is dominant during the injection event of the injector studied. When string cavitation appears by a counter-rotating vortex pair centered at the hole entrance, no shear-cavitation is usually observed. The reduction or the collapse of the vortex pair favors the direct flow from the inlet to turn, separate and a shear-cavitation regime can temporarily develop. As the vortex pair is observed again, shear-cavitation disappears. String and shear cavitation rarely appear together: this happens only if a single cavitating vortex is present (t $\in [189, 191]\,\mu$s) or rarely in short time intervals (t $\in [157, 159]\,\mu$s). At t= 197 μs, shear cavitation is followed by a string that will cavitate at the nozzle hole end; then, this small vortex will merge with the main strings at time t=199 μs.

A remark about the visual classification of cavitation is finally due, with specific reference to the time interval [119, 129] μs. Cavitating vortices can move freely while shear cavitation is geometric-driven. A cavitating vortex can move toward the wall of the nozzle hole, can reach the proximity of the wall (t $\in$ [119,121]), then shear and string cavitation disappear. The process restarts in the time interval [127, 129]. From the observations, cavitation seems always to originate from shear cavitation; then, it is driven by a vortex and it does not exhibit the same kinematic features of the classical shear cavitation. High-fidelity simulations suggest that additional care is required when classifying the type of cavitation (shear vs string) from the analysis of the images.

10. Conclusion

A three-phase LES solver [28] has been used to carry out a study about the evolution of string cavitation on two transparent nozzle replicas of real high pressure injectors, namely configurations ID-3 and ID-10. Both geometries represent one sixth of a sector with a multi-hole injector. The different performance of ID-10 and ID-3 is due to their geometrical features (e.g nozzle diameters, height, dead spaces) and to the inlet flow conditions developing from the small details in the sac. The agreement between simulations and experimental visualizations of the cavitating flow observed by two views (frontal and side) is satisfying. Validated results have been then used to analyze the nozzle flow fields. Results are somehow unexpected. The flow pattern in both injectors is almost symmetric and presents a large recirculating region in the sac generating a pair of counter-rotating eddies in the region between the upper wall of the sac and the hole entrance. Despite the different sac geometry of the two samples, flow features at the nozzle entrance are similar, as evidenced by the values of the parameter r of Eq. (11).. While r is used to characterize the flow behavior in the sac, the conicity is used for the hole only. Injector ID-10 presents a shorter hole and a lower conicity; its mean pressure level and the intensity of the flow recirculation (identified by the ratio between the non-axial and the axial kinetic energy), as well as the amount of vapor produced at the nozzle outlet, are the largest for this injector geometry. From the present study it is shown that non-axial kinetic energy in the nozzle seems to be a more relevant parameter with respect to vorticity to characterize the motion of large structures and the intensity of the in-nozzle cavitation. On the other hand, no conclusive remarks to optimize the injector design can be still drawn: the size and distribution of the maximum ligaments out of the nozzle exit and the spatial dispersion/homogeneity of the spray in the outer region are some of the additional relevant parameters that must also be taken into account. These parameter are related to the study of the primary atomization, that will be the topic of upcoming publications.

Finally, a pseudo-periodic appearance of string and shear cavitation has been observed from the simulations. It has been shown that string and shear cavitation can coexist. The occurrence of shear and string cavitation is the result of different superimposing types of flow motions. In the sac, a secondary motion is superposed on the primary flow with the fluid coming from the inlet channel and the fluid deviated inside the sac volume being swept towards the

nozzle hole entrance. This kind of flow promotes string cavitation, but in principle it does not generate enough flow detachment for shear cavitation to develop. On the other hand, flow unsteadiness and vortex pair instabilities make string vortexes in the nozzle hole merge or move towards the walls and brake. As a consequence, the flow topology may change and the rate of cavitation of the fuel is temporarily dominated by the classical shear cavitation in the liquid shear layer forming at the hole entrance. In between of these two extreme conditions, a wide range of complex interaction between string and shear cavitation has been observed.

11. Acknowledgments

Authors gratefully acknowledge the Laboratory Computing Resource Center (LCRC) at Argonne National Laboratory for the computing resources provided through the `KNL-OpenFOAM-VOF` project. Authors would like to thank also Mr. Louis-Philippe Elie, Dr. Stefan Schuster and Dr. Eberhard Kull for the support received on the transparent nozzle manufacturing. The code used for the simulations, including automatic pre- and post-processing, is part of the LibPoliMi/DAER code, an open-source C++ library developed by the authors at the Dept. of Aerospace Science and Technology, Politecnico di Milano (DAER-PoliMi) based on the OpenFOAM Technology (OpenFOAM-8 and OpenFOAM-dev, `commit 4c08b463f`). Argonne National Laboratory's work was supported in part by the U.S. Department of Energy Office of Science, under contract DE-AC02-06CH11357.

References

[1] B. Yin, S. Yu, H. Jia, J. Yu, Numerical research of diesel spray and atomization coupled cavitation by large eddy simulation (les) under high injection pressure, International Journal of Heat and Fluid Flow 59 (2016) 1 – 9. doi:https://doi.org/10.1016/j.ijheatfluidflow.2016.01.005.
URL `http://www.sciencedirect.com/science/article/pii/S0142727X16300029`

[2] S. Makhlouf, J. Hélie, G. Grimoux, J. Cousin, L. Gestri, A. Wood, G. Wigley, Large eddy simulation of cavitation and atomization in injector flows using openfoam, in: ICLASS 2012, 12th Triennial Int. Conference on Liquid Atomization and Spray Systems, Heidelberg, Germany, 2012.

[3] O. J. Soriano-Palao, M. Sommerfeld, A. Burkhardt, Modelling the influence of the nozzle geometry on the primary breakup of diesel jets, International Journal of Spray and Combustion Dynamics 6 (2) (2014) 113–146. doi:10.1260/1756-8277.6.2.113.
URL `https://doi.org/10.1260/1756-8277.6.2.113`

[4] R. Torelli, S. Som, Y. Pei, Y. Zhang, M. Traver, Influence of fuel properties on internal nozzle flow development in a multi-hole diesel injector, Fuel 204 (2017) 171 – 184. doi:https://doi.org/10.1016/j.fuel.2017.04.123.
URL `http://www.sciencedirect.com/science/article/pii/S0016236117305446`

[5] F. Piscaglia, F. Giussani, A. Montorfano, J. Hélie, S. Aithal, A multiphase dynamic-vof solver to model primary jet atomization and cavitation inside high-pressure fuel injectors in openfoam, Acta Astronauticadoi:https://doi.org/10.1016/j.actaastro.2018.07.026.

[6] Hannebique, G. and Sierra, P. and Riber, E. et al., Large Eddy Simulation of Reactive Two-Phase Flow in an Aeronautical Multipoint Burner., Flow Turbulence Combustion 90 (2013) 449–469.

[7] A. Sou, B. Biçer, A. Tomiyama, Numerical simulation of incipient cavitation flow in a nozzle of fuel injector, Computers & Fluids 103 (2014) 42–48. doi:https://doi.org/10.1016/j.compfluid.2014.07.011.

[8] A. Sou, S. Hosokawa, A. Tomiyama, Effects of cavitation in a nozzle on liquid jet atomization, International Journal of Heat and Mass Transfer 50 (17) (2007) 3575 – 3582. doi:https://doi.org/10.1016/j.ijheatmasstransfer.2006.12.033.
URL `http://www.sciencedirect.com/science/article/pii/S0017931007001019`

[9] P. Aleiferis, Y. Hardalupas, D. Kolokotronis, A. Taylor, A. Arioka, M. Saito, Experimental investigation of the internal flow field of a model gasoline injector using micro-particle image velocimetry, in: Powertrain & Fluid Systems Conference and Exhibition, SAE International, 2006. doi:https://doi.org/10.4271/2006-01-3374.
URL `https://doi.org/10.4271/2006-01-3374`

[10] P. Aleiferis, Y. Hardalupas, D. Kolokotronis, A. Taylor, T. Kimura, Investigation of the internal flow field of a diesel model injector using particle image velocimetry and cfd, in: JSAE/SAE International Fuels & Lubricants Meeting, SAE International, 2007. doi:https://doi.org/10.4271/2007-01-1897.
URL `https://doi.org/10.4271/2007-01-1897`

[11] H. Chaves, R. Knake, R. Miranda, Particle image velocimetry measurements of the cavitating flow in a real size transparent vco nozzle, in: ICMF-2007 - 6th Int. Conference on Multiphase Flow, Leipzig, Germany, 2007.

[12] H. Watanabe, M. Nishikori, T. Hayashi, M. Suzuki, N. Kakehashi, M. Ikemoto, Visualization analysis of relationship between vortex flow and cavitation behavior in diesel nozzle, Int. Journal of Engine Research (1) (2014) 5–12.

[13] A. Ahmed, B. Duret, J. Reveillon, F. Demoulin, Numerical simulation of cavitation for liquid injection in non-condensable gas, International Journal of Multiphase Flow 127 (2020) 103269. doi:https://doi.org/10.1016/j.ijmultiphaseflow.2020.103269.

[14] S. Jollet, H. Hansen, K. Bitner, D. Niemeyer, F. Dinkelacker, Experimental and numerical investigations of 90 μm real-size transparent nozzles with high pressure conditions, in: ILASS Europe, 26th Annual Conference on Liquid Atomization and Spray Systems, 8-10 Sep. 2014, Bremen, Germany, 2014.

[15] Z. Chen, Z. He, W. Shang, L. Duan, H. Zhou, G. Guo, W. Guan, Experimental study on the effect of nozzle geometry on string cavitation in real-size optical diesel nozzles and spray characteristics, Fuel 232 (2018) 562 – 571. doi:https://doi.org/10.1016/j.fuel.2018.05.132.
URL `http://www.sciencedirect.com/science/article/pii/S0016236118309670`

[16] A. Andriotis, M. Gavaises, Influence of vortex flow and cavitation on near-nozzle diesel spray dispersion angle, Atomization and Sprays 19 (3) (2009) 247–261.

[17] L. C. Ganippa, G. Bark, S. Andersson, J. Chomiak, Cavitation: a contributory factor in the transition from symmetric to asymmetric jets in cross-flow nozzles, Experiments in Fluids 36 (4) (2004) 627–634. doi:10.1007/s00348-003-0736-4.
URL https://doi.org/10.1007/s00348-003-0736-4
[18] B. A. Reid, G. K. Hargrave, C. P. Garner, G. Wigley, An investigation of string cavitation in a true-scale fuel injector flow geometry at high pressure, Physics of Fluids 22 (3) (2010) 031703. arXiv:https://doi.org/10.1063/1.3372174, doi:10.1063/1.3372174.
URL https://doi.org/10.1063/1.3372174
[19] B. Reid, M. Gavaises, N. Mitroglou, G. Hargrave, C. Garner, E. Long, R. McDavid, On the formation of string cavitation inside fuel injectors, Experiments in Fluids 55 (1).
[20] M. Gavaises, A. Andriotis, D. Papoulias, N. Mitroglou, A. Theodorakakos, Characterization of string cavitation in large-scale diesel nozzles with tapered holes, Physics of Fluids 21 (5).
[21] A. Papoutsakis, A. Theodorakakos, E. Giannadakis, D. Papoulias, Les predictions of the vortical flow structures in diesel injector nozzles, SAE Technical Paper 2009-01-0833.
[22] S. Clerc, Numerical simulation of the homogeneous equilibrium model for two-phase flows, Journal of Computational Physics 161 (1) (2000) 354 – 375. doi:https://doi.org/10.1006/jcph.2000.6515.
[23] B. R. Parkin, Scale effects in cavitating flow, Ph.D. thesis, California Institute of Technology (1952).
[24] E. Winklhofer, E. Kull, E. Kelz, A. Morozov, Comprehensive hydraulic and flow field documentation in model throttle experiments under cavitation conditions, in: ILASS 2001, 17th European Conference on Liquid Atomization and Spray Systems, Zurich, Switzerland, 2001.
[25] C. Mauger, L. Méès, M. Michard, A. Azouzi, S. Valette, Shadowgraph, Schlieren and interferometry in a 2D cavitating channel flow, Experiments in Fluids 53 (6) (2012) 1895–1913. doi:10.1007/s00348-012-1404-3.
URL https://hal.archives-ouvertes.fr/hal-00780132
[26] R. Payri, F. Salvador, J. Gimeno, O. Venegas, Study of cavitation phenomenon using different fuels in a transparent nozzle by hydraulic characterization and visualization, Experimental Thermal and Fluid Science 44 (2013) 235 – 244. doi:https://doi.org/10.1016/j.expthermflusci.2012.06.013.
URL http://www.sciencedirect.com/science/article/pii/S089417771200177X
[27] W. H. Nurick, Orifice cavitation and its effect on spray mixing, Journal of Fluids Engineering 98 (4) (1976) 681. doi:10.1115/1.3448452.
URL https://doi.org/10.1115/1.3448452
[28] F. Giussani, F. Piscaglia, G. Saez-Mischlich, J. Hèlie, A three-phase VOF solver for the simulation of in-nozzle cavitation effects on liquid atomization, Journal of Computational Physics (2019) 109068doi:https://doi.org/10.1016/j.jcp.2019.109068.
[29] A. Agresta, J. Hélie, E. Kull, N. Lamarque, A. Lyubar, S. Schuster, Real-Size Real-Shape Real-Pressure Transparent Nozzles to Contribute to Nozzle Design and Cavitation Control for GDI, in: 29th Conference on Liquid Atomization and Spray Systems, ILASS-Europe, 2-4 September 2019, Paris, France.
[30] J. M. Shi, K. Wenzlawski, J. Helie, H. Nuglish, J. Cousin, Urans ans sas analysis of flow dynamics in a gdi nozzle, in: ILASS – Europe 2010, 23rd Annual Conference on Liquid Atomization and Spray Systems, Brno, Czech Republic, September 2010, 2010.
[31] M. Gavaises, A. Andriotis, D. Papoulias, N. Mitroglou, A. Theodorakakos, Characterization of string cavitation in large-scale diesel nozzles with tapered holes, Physics of Fluids 21 (5) (2009) 052107. doi:10.1063/1.3140940.
[32] H. Chaves, M. Knapp, A. Kubitzek, F. Obermeier, et al., Experimental study of cavitation in the nozzle hole of diesel injectors using transparent nozzles, SAE Technical Paper 950290.
[33] U. Iben, A. Morozov, E. Winklhofer, F. Wolf, Laser-pulse interferometry applied to high-pressure fluid flow in micro channels, Experiments in Fluids 50 (3) (2011) 597–611.
[34] J. Serras-Pereira, Z. van Romunde, P. Aleiferis, D. Richardson, S. Wallace, R. Cracknell, Cavitation, primary break-up and flash boiling of gasoline, iso-octane and n-pentane with a real-size optical direct-injection nozzle, Fuel 89 (9) (2010) 2592 – 2607. doi:https://doi.org/10.1016/j.fuel.2010.03.030.
URL http://www.sciencedirect.com/science/article/pii/S0016236110001225
[35] A. SOU, M. M. Ilham, K. ISOZAKI, S. HOSOKAWA, A. TOMIYAMA, Effects of nozzle geometry on cavitation in nozzles of pressure atomizers, Journal of Fluid Science and Technology 3 (5) (2008) 622–632. doi:10.1299/jfst.3.622.
URL https://ci.nii.ac.jp/naid/130000077343/en/
[36] J. Cui, H. Lai, K. Feng, Y. Ma, Quantitative analysis of the minor deviations in nozzle internal geometry effect on the cavitating flow, Experimental Thermal and Fluid Science 94 (2018) 89 – 98. doi:https://doi.org/10.1016/j.expthermflusci.2018.02.002.
URL http://www.sciencedirect.com/science/article/pii/S0894177718301377
[37] E. Roohi, A. P. Zahiri, M. Passandideh-Fard, Numerical simulation of cavitation around a two-dimensional hydrofoil using vof method and les turbulence model, Applied Mathematical Modelling 37 (9) (2013) 6469 – 6488. doi:http://dx.doi.org/10.1016/j.apm.2012.09.002.
[38] E. Kawakami, R. Arndt, Investigation of the behavior of ventilated supercavities, ASME. J. Fluids Eng. 133 (9). doi:10.1115/1.4004911.
[39] J. H. Kim, K. Nishida, H. Hiroyasu, Characteristics of the internal flow in a diesel injection nozzle, Int. Journal of Fluid Mechanics Research 24 (1-3) (1997) 34–44.
[40] R. Husson, L. Ganippa, H. Zhao, Flow and cavitation structure in a scaled-up multi hole optical diesel nozzle, in: 22nd European Conference on Liquid Atomization and Spray Systems (ILASS), 8-10 September 2008, Como (Italy), 2008.
[41] G. L. Chahine, Bubble Interactions with Vortices, Springer Netherlands, Dordrecht, 1995, pp. 783–828. doi:10.1007/978-94-011-0249-0_18.
URL https://doi.org/10.1007/978-94-011-0249-0_18
[42] W. Bergwerk, Flow pattern in diesel nozzle spray holes, Proceedings of the Institution of Mechanical Engineers 173 (1) (1959) 655–660.
[43] J. Sauer, G. H. Schnerr, Unsteady cavitating flow: A new cavitation model based on modified front capturing method and bubble dynamics (2000 2000).
[44] W. Yuan, J. Sauer, G. H. Schnerr, Modeling and computation of unsteady cavitation flows in injection nozzles, Mécanique & Industries 2 (5) (2001) 383 – 394. doi:http://dx.doi.org/.
[45] C. Hirt, B. Nichols, Volume of fluid (vof) method for the dynamics of free boundaries, Journal of Computational Physics 39 (1) (1981) 201 – 225. doi:https://doi.org/10.1016/0021-9991(81)90145-5.
[46] The OpenFOAM Foundation, OpenFOAM User Guide.
URL https://cfd.direct/openfoam/user-guide
[47] R. Issa, Solution of the implicitly discretised fluid flow equations by operator-splitting, Journal of Computational Physics 62 (1) (1986) 40 – 65. doi:https://doi.org/10.1016/0021-9991(86)90099-9.

URL http://www.sciencedirect.com/science/article/pii/0021999186900999
[48] H. Weller, A new approach to VOF-based interface capturing methods for incompressible and compressible flow, Technical report TR/HGW/04, OpenCFD Ltd. (2008).
[49] P. Koukouvinis, H. Naseri, M. Gavaises, Performance of turbulence and cavitation models in prediction of incipient and developed cavitation, International Journal of Engine Research 18 (4) (2017) 333–350. arXiv:https://doi.org/10.1177/1468087416658604, doi:10.1177/1468087416658604.
URL https://doi.org/10.1177/1468087416658604
[50] M. Gavaises, F. Villa, P. Koukouvinis, M. Marengo, J.-P. Franc, Visualisation and les simulation of cavitation cloud formation and collapse in an axisymmetric geometry, International Journal of Multiphase Flow 68 (2015) 14 – 26. doi:https://doi.org/10.1016/j.ijmultiphaseflow.2014.09.008.
URL http://www.sciencedirect.com/science/article/pii/S0301932214001700
[51] R. E. Bensow, G. Bark, Implicit LES predictions of the cavitating flow on a propeller, Journal of Fluids Engineering 132 (4) (2010) 041302. doi:10.1115/1.4001342.
URL https://doi.org/10.1115/1.4001342
[52] X. Luo, B. Ji, X. Peng, H. Xu, M. Nishi, Numerical simulation of cavity shedding from a three-dimensional twisted hydrofoil and induced pressure fluctuation by large-eddy simulation, Journal of Fluids Engineering 134 (4) (2012) 041202. doi:10.1115/1.4006416.
URL https://doi.org/10.1115/1.4006416
[53] Y. Chen, X. Chen, J. Li, Z. Gong, C. Lu, Large eddy simulation and investigation on the flow structure of the cascading cavitation shedding regime around 3d twisted hydrofoil, Ocean Engineering 129 (2017) 1 – 19. doi:https://doi.org/10.1016/j.oceaneng.2016.11.012.
URL http://www.sciencedirect.com/science/article/pii/S0029801816305121
[54] B. Huang, Y. Zhao, G. Wang, Large eddy simulation of turbulent vortex-cavitation interactions in transient sheet/cloud cavitating flows, Computers & Fluids 92 (2014) 113 – 124. doi:https://doi.org/10.1016/j.compfluid.2013.12.024.
URL http://www.sciencedirect.com/science/article/pii/S0045793013005161
[55] B. Ji, X. Luo, R. E. Arndt, X. Peng, Y. Wu, Large eddy simulation and theoretical investigations of the transient cavitating vortical flow structure around a naca66 hydrofoil, International Journal of Multiphase Flow 68 (2015) 121 – 134. doi:https://doi.org/10.1016/j.ijmultiphaseflow.2014.10.008.
URL http://www.sciencedirect.com/science/article/pii/S0301932214001967
[56] J. Reboud, B. Stutz, O. Coutier, Two-phase flow structure of cavitation:experiments and modelling of unsteady effects, in: 3rd International Symposium on Cavitation, april 1998, Grenoble, France, 1998.
[57] O. Coutier-Delgosha, R. Fortes-Patella, J. L. Reboud, Evaluation of the turbulence model influence on the numerical simulations of unsteady cavitation, Journal of Fluids Engineering 125 (1) (2003) 38. doi:10.1115/1.1524584.
URL https://doi.org/10.1115/1.1524584
[58] B. Huang, A. Ducoin, Y. L. Young, Physical and numerical investigation of cavitating flows around a pitching hydrofoil, Physics of Fluids 25 (10) (2013) 102109. doi:10.1063/1.4825156.
URL https://doi.org/10.1063/1.4825156
[59] B. Huang, Y. L. Young, G. Wang, W. Shyy, Combined experimental and computational investigation of unsteady structure of sheet/cloud cavitation, Journal of Fluids Engineering 135 (7) (2013) 071301. doi:10.1115/1.4023650.
URL https://doi.org/10.1115/1.4023650
[60] Y. Long, X. ping Long, B. Ji, W. xin Huai, Z. dong Qian, Verification and validation of urans simulations of the turbulent cavitating flow around the hydrofoil, Journal of Hydrodynamics, Ser. B 29 (4) (2017) 610 – 620. doi:https://doi.org/10.1016/S1001-6058(16)60774-6.
URL http://www.sciencedirect.com/science/article/pii/S1001605816607746
[61] D. Dietzel, D. Messig, F. Piscaglia, A. Montorfano, G. Olenik, O. T. Stein, A. Kronenburg, A. Onorati, C. Hasse, Evaluation of scale resolving turbulence generation methods for large eddy simulation of turbulent flows, Computers & Fluids 93 (2014) 116 – 128. doi:https://doi.org/10.1016/j.compfluid.2014.01.013.
URL http://www.sciencedirect.com/science/article/pii/S0045793014000206
[62] D. Fuster, A. Bagué, T. Boeck, L. L. Moyne, A. Leboissetier, S. Popinet, P. Ray, R. Scardovelli, S. Zaleski, Simulation of primary atomization with an octree adaptive mesh refinement and vof method, International Journal of Multiphase Flow 35 (6) (2009) 550 – 565. doi:https://doi.org/10.1016/j.ijmultiphaseflow.2009.02.014.
URL http://www.sciencedirect.com/science/article/pii/S0301932209000305
[63] Y. Wu, A. Montorfano, F. Piscaglia, A. Onorati, A Study of the Organized in-Cylinder Motion by a Dynamic Adaptive Scale-Resolving Turbulence Model, Flow, Turbulence and Combustion.
[64] A. Montorfano, F. Piscaglia, A. Onorati, An Extension of the Dynamic Mesh Handling with Topological Changes for LES of ICE in OpenFOAM, SAE Technical Paper 2015-01-0384.
[65] A. Andriotis, M. Gavaises, C. Arcoumanis, Vortex flow and cavitation in diesel injector nozzles, Journal of Fluid Mechanics 610 (2008) 195–215.
[66] B. A. Reid, G. K. Hargrave, C. P. Garner, G. Wigley, An investigation of string cavitation in a true-scale fuel injector flow geometry at high pressure, Physics of Fluids 22 (3) (2010) 031703. arXiv:https://doi.org/10.1063/1.3372174, doi:10.1063/1.3372174.
URL https://doi.org/10.1063/1.3372174